The TRIple-frequency and Polarimetric radar Experiment for improving process observation of winter precipitation

José Dias Neto[1], Stefan Kneifel[1], Davide Ori[1], Silke Trömel[2], Jan Handwerker[3], Birger Bohn[4], Normen Hermes[5], Kai Mühlbauer[2], Martin Lenefer[2], and Clemens Simmer[2]

[1]Institute for Geophysics and Meteorology, University of Cologne, Cologne, Germany
[2]Institute for Geosciences and Meteorology, University of Bonn, Bonn, Germany.
[3]Institute of Meteorology and Climate Research (IMK), Karlsruhe Institute of Technology (KIT), Karlsruhe, Germany
[4]Institute of Energy and Climate Research (IEK-8), Research Centre Jülich, Jülich, Germany
[5]Institute of Bio- and Geosciences Agrosphere (IBG-3), Research Centre Jülich, Jülich, Germany

Correspondence: José Dias (jdiasnet@uni-koeln.de)

Abstract. This ~~study describes a two-months~~ paper describes a two-month dataset of ground-based triple-frequency (X, Ka, and ~~W-Band) Doppler cloud~~ W Band) Doppler radar observations during the winter season obtained at the Jülich ObservatorY for Cloud Evolution ~~core facility~~ Core Facility (JOYCE-CF), Germany. All relevant post-processing steps, such as re-gridding, offset and attenuation correction, as well as quality flagging are described. The dataset contains all ~~information needed~~ necessary information required to recover data at intermediate processing steps for user-specific applications and corrections (~~DOI: 10.5281/zenodo.1405539~~https://doi.org/10.5281/zenodo.1341389). The ~~rather long time duration of the dataset allowed for a statistical analysis, which we focused on the ice and snow part of the cloud~~large number of ice clouds included in the dataset allows for a first statistical analysis of their multi-frequency radar signatures. The reflectivity differences quantified by dual-wavelength ratios ~~revealed~~ (DWR) reveal temperature regimes, where aggregation seems to be triggered. Overall, the aggregation signatures found in the triple-frequency space agree with and corroborate conclusions from previous studies. ~~Combining the information from reflectivity information~~ The combination of DWR with mean Doppler velocity and linear depolarization ratio ~~,~~ enables us to distinguish signatures of rimed particles and melting snowflakes~~; while the riming signatures~~ . The riming signatures in the DWR agree well with results ~~from previous studies~~found in previous triple-frequency studies. Close to the melting layer, however, we find very ~~strong aggregation signatures close to the melting layer~~large DWR (up to 20 dB), which have not been reported before. ~~Mean~~ A combined analysis of these extreme DWR with mean Doppler velocity and ~~the~~ linear depolarization ratio ~~have been used to separate the extreme aggregation signature~~allows to separate this signature, which is most likely related to strong aggregation, from the triple-frequency characteristics of melting particles.

1 Introduction

The combined observation of clouds and precipitation at different radar frequencies ~~potentially improves the particle type and quantity retrieval accuracy because their~~ is used to improve retrievals of hydrometeor properties. All methods exploit frequency-dependent hydrometeor scattering and absorption properties ~~depend on the particle microphysical characteristicsand electromagnetic frequency. One example is the retrieval of vertical profiles of cloud liquid water content from the~~ governed by their microphysical characteristics.

Multi-frequency retrievals are already well developed for liquid hydrometeors. For example, Hogan et al. (2005) used differential radar attenuation at 35 and 94 GHz ~~(e.g. Hogan et al. (2005)) and the retrieval of precipitation rates from the Ku-Ka-Band dual-frequency radar on~~ to retrieve vertical profiles of cloud liquid water. Improved precipitation rate retrievals on a global scale are provided by the core satellite of the Global Precipitation Mission ~~(GPM, Hou et al. (2014))~~which operates a Ku-Ka Band dual-frequency radar (Hou et al., 2014). For frequencies below ≈10 GHz, attenuation effects are ~~very small~~ negligible (except for heavy rainfall or hail) ~~but~~ and the sensitivity to non-precipitating particles~~is~~ , such as ice crystals, is relatively weak. Therefore, the majority of multi-frequency applications for cold clouds ~~focus~~ focuses on cloud radar systems operating ~~usually~~ at 35 GHz or 94 GHz~~which provide enhanced sensitivity even to~~ . At these frequencies, the radars are sensitive enough to detect even sub-millimeter ice particles and cloud droplets. The ~~microwave scattering properties of frozen hydrometeors such as~~ sizes of large ice crystals, snowflakes, graupel, and hail ~~lie in this frequency range within the transition zone between Rayleigh and Mie scattering regimes~~are in the order of the wavelengths used to observe them (3mm, 8mm, 3cm for W, Ka, and X Band, respectively). Thus, ~~this size-dependent scattering effect~~ non-Rayleigh scattering becomes important and can be used to ~~improve the estimates of ice water content and characteristic particle size distribution (PSD) (Matrosov, 1998; Hogan et al., 2000)~~constrain particle size distributions, improving ice and snow water content retrievals (Matrosov, 1998; Hogan et al., 2000; Leinonen et al., 2018; Grec

Recent modeling studies ~~(Kneifel et al., 2011b; Tyynelä and Chandrasekar, 2014; Leinonen and Moisseev, 2015; Leinonen and Szyrmer~~ that different ice particle classes like graupel, single crystals, or aggregates, can be distinguished using a combination of three radar frequencies (13, 35 and 94 GHz). ~~Early triple-frequency~~ Triple-frequency radar datasets from airborne campaigns (Leinonen et al., 2012; Kulie et al., 2014) and satellites (Yin et al., 2017) confirmed distinct signatures ~~of the various ice hydrometeor classes~~ in the triple frequency space. Ground-based triple-frequency radar measurements in combination with in-situ observations (Kneifel et al., 2015) provided the first experimental evidence for a close relation between triple-frequency signatures and the characteristic particle size, as well as the bulk density of snowfall. ~~Methods which utilize the information content of the~~ These early results were corroborated and refined by coinciding in-situ observations in aircraft campaigns (Chase et al., 2018) as well as by ground-based observations (Gergely et al., 2017). A better understanding of the relations between triple-frequency ~~Doppler spectrum are still under developmentbut first analyses show already their potential e.g. to constrain snow particle scattering models (Kneifel et al., 2016).~~ signatures and snowfall properties are key for triple-frequency radar retrieval development. The connection between scattering and microphysical properties is currently addressed by novel ground-based in-situ instrumentation (Gergely et al., 2017) and triple-frequency Doppler spectra (Kneifel et al., 2016). Long-term

triple-frequency datasets from various sites and radar systems are, however, needed to better understand the relations between triple-frequency signatures and clouds.

In this article, we We present a first analysis of two months winter triple-frequency (X, Ka, W-BandW Band) radar observations collected over two winter months at the Jülich observatory for cloud evolution core facility, Germany (Löhnert et al., 2015). Particular effort has been taken to correct the data The data were corrected for known offsets and attenuation as well as to re-grid the dataset to allow its convenient use effects and re-gridded for multi-frequency analysesstudies. Section 2 describes the experimental campaign setup and the characteristics of the X, Ka and W band radarsused during the experimentBand radars. Section 3 gives a detailed description of details the data processing , corrections appliedand remaining limitations of the data. Section and corrections applied. Section 4 gives a general overview of the dataset and its limitations. Section 5 presents a statistical analysis of the data where a with a focus on the temperature dependency of the triple-frequency signatures is identified. In additionproperties, signatures of riming, intense aggregation, and melting snow particlesare presented.. We summarize and discuss our results in Section 6.

2 Measurement Site and Instruments

The "TRIple-frequency and Polarimetric radar Experiment for improving process observation of winter precipitation" (TRIPEx) was a joint field experiment of the University of Cologne, the University of Bonn, the Karlsruhe Institute of Technology (KIT), and the Jülich Research Centre (Forschungszentrum Jülich, FZJ). TRIPEx took place at the Jülich Observatory for Cloud Evolution Core Facility (JOYCE-CF ,–$50°54'31''N, 6°24'49''E$, 111 m above mean sea level; Löhnert et al. (2015)) from 11 November 2015 until 04 January 2016. The core instruments deployed during TRIPEx were three vertically pointing radars providing a triple-frequency (X-Band, Ka-Band, and W-BandX, Ka, and W Band) column view of the hydrometeors aloft. All three radars were calibrated by the manufacturers before the campaign. Figure 1 shows a simplified diagram sketches the positions of the instruments relative deployment positions. In addition to the three radars, a to each other and the ground surface. A large number of additional permanently installed remote sensing and in-situ observing instruments are available at the JOYCE-CF site (see Löhnert et al. (2015) for a detailed overview).

2.1 Precipitation Radar KiXPol (X-BandX Band)

KiXPol KiXPol, hereafter referred to X Band, is a pulsed X-band 9.4 GHz Doppler precipitation radar, normally usually integrated into the KITcube platform (Kalthoff et al., 2013). The mobile Meteor 50DX radar, manufactured by Selex ES (Gematronik), is mounted on a trailer and placed next to the JOYCE-CF building in order to position it as close as possible to the other two radars, which were installed on the JOYCE-CF roof-platform (see Figure 1). KiXPol operates at 9.4 The radar operates in a simultaneous transmit and receive (STAR) mode and is thus capable to measure of measuring standard polarimetric variables like differential reflectivity Z_{dr} and differential phase shift Φ_{dp}, but not the linear depolarization ratio LDR which . Linear depolarization ratio (LDR) is not provided because it requires the emission of single-polarization pulses in order to allow for independent measurements of the cross-polarized component of the returning signal. Due to the zenith only operation

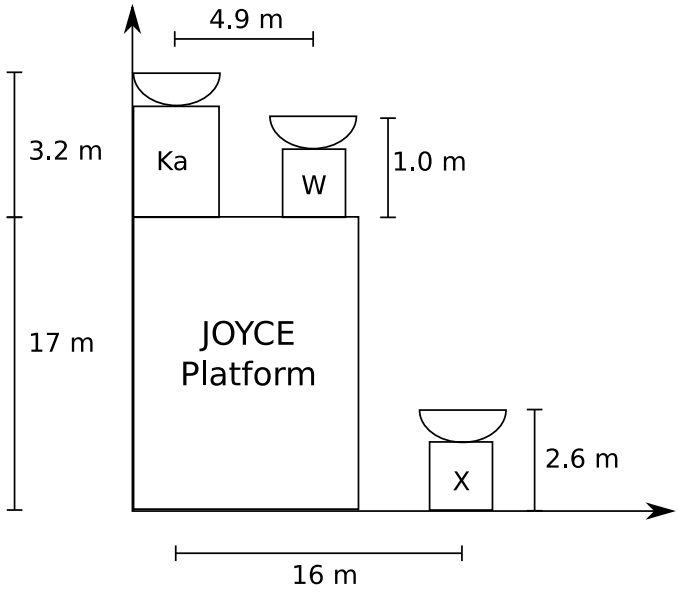

Figure 1. Sketch (not to scale) of the horizontal and vertical distances ~~of~~ between the three zenith-pointing radars operated during TRIPEx. The JOYCE-CF platform with all auxiliary instruments is located on the roof of a 17 m tall building. The mobile ~~X-Band~~ X Band radar was placed on the ground ~~as~~ close ~~as possible~~ to the other two radars.

~~during~~ During the campaign, the ~~KiXPol polarimetric variables available from its STAR-mode operation do not contain relevant information about the hydrometeors and are thus not included in the dataset. Using~~ X Band was set to a pulse duration of 0.3 µs~~, we set the radial resolution down to~~ ; a slight oversampling was applied to achieve a radial resolution of 30 m ~~which is close to~~ in order to match the resolution of the other radars as close as possible (see Table 1). ~~Since KiXPol~~ The X Band radar is designed for operational observations of precipitation via volume scans (series of azimuth scans at several fixed elevation angles)~~the~~ . KiXPol was operated at JOYCE in this mode during the HOPE campaign (Xie et al., 2016; Macke et al., 2017). The standard software requires to rotate the antenna in azimuth in order to record data. Hence, we constantly rotated the antenna at zenith elevation with a slow rotation speed ($2°s^{-1}$) in order to enhance the sensitivity ~~due to~~ by a longer time averaging. After each complete rotation, ~~a gap of a few seconds interrupts the measurement~~ the radar stops the measurements for few seconds before the next scan ~~was started~~starts, introducing thus a small measurement gap at each scan routine. Further technical specifications ~~about the KiXPol can be found~~ of X Band are listed in Table 1.

2.2 Cloud Radar JOYRAD-35 (~~Ka-Band~~Ka Band)

JOYRAD-35, hereafter referred to Ka Band, is a scanning ~~Ka-Band~~ 35.5 GHz Doppler cloud radar of the type MIRA-35 (Görsdorf et al., 2015) manufactured by ~~METEK~~ Metek (Meteorologische Messtechnik GmbH), Germany. An overview of its main technical characteristics and settings used during TRIPEx is provided in Table 1. ~~JOYRAD-35~~ The radar transmits linearly polarized pulses at 35.5 GHz and receives simultaneously the co- and cross-polarized returns~~; thus the linear depolarization~~

ratio LDRcan be derived. This allows to derive LDR, which is used e.g. by the Metek processing software to filter out signals from insects and to detect the melting layerby the Metek processing software. From the measured Doppler spectra, standard radar moments such as effective reflectivity factor Ze, mean Doppler velocity MDV (MDV) and Doppler spectral width SW (SW) are computed. Since March 2012, JOYRAD-35 the Ka Band radar is a permanent component of the JOYCE-CF site (Löhnert et al., 2015)(Löhnert et al., 2015), and its zenith observations are used as input for generating CloudNet products (Illingworth et al., 2007). As the main The radar was vertically pointing most of the time because the major scientific focus during TRIPEx was to collect combined triple-frequency observations, JOYRAD-35 was vertically pointing most of the time. Every 30 minutesit performed , a sequence of Range Height Display (RHI) scans at different azimuth directions (duration $\approx$ 4 minutes) was performed in order to capture a snapshot of the spatial cloud field, and also to derive the radial component of the horizontal wind inside the cloud. As the The scanning data has not been processed yet, the current dataset ; thus, the dataset described here only includes the zenith observationsand ; the RHI scans will be included in a future release. JOYRAD-35 The Ka Band radar was almost continuously operating during the TRIPEx campaign, except for a gap from 25th of November to 2^{sdnd} of December 2015 that was related to a hard disk failure due to a failure of the storage unit.

2.3 Cloud Radar JOYRAD-94 (W-BandW Band)

JOYRAD-94, hereafter referred to W Band, is a 94 GHz, frequency modulated continuous wave (FMCW) radar, combined with a radiometric channel at 89 GHz. The instrument is manufactured by Radiometer Physics GmbH (RPG), Germany. Unlike the previously introduced two radars, JOYRAD-94 X and Ka Band radar, the W Band radar is a non-polarimetric, non-scanning and non-pulsed radar system. JOYRAD-94 is continuously operating system. W Band started measurements at JOYCE-CF since in October 2015; a detailed description of the radar performance, hardware, signal processing, and calibration can be found in Küchler et al. (2017). As summarized in Table 1, JOYRAD-94 The W Band radar has a similar beam-widthas well as range, range, and temporal resolution as JOYRAD-35. Unlike for the pulsed radars, the JOYRAD-94 range resolution is not fixed, but depends on the gate distance as a consequence of the use of different FMCW chirp settings for different heights. We used Ka Band (Table 1). The FMCW system allows the user to set different range resolutions for different altitude by acting on the frequency modulation settings (chirp sequence). During TRIPEx the standard chirp table sequence (Table 2) as described in Küchler et al. (2017) which has different range resolutions, Nyquist velocities, and sensitivities for the different height ranges. The measured Doppler spectra are first corrected for aliasing (Küchler et al., 2017), and has been used. After correcting the Doppler spectra for aliasing using the method described in Küchler et al. (2017), standard radar moments such as the equivalent Ze, MDV and SW are derivedfrom them.

3 Data processing

The full TRIPEx dataset is stored in three different levels of processing structured on three processing levels. Level 0 contains the original data from JOYRAD-35, JOYRAD-94 and KixPolX, Ka and W Band. For Level 1the measurements were , the measurements are corrected for known instrument problems and were formatted sampled into a common time-height

Table 1. Technical specifications and settings of the three vertically pointing radars operated during TRIPEx at JOYCE-CF.

Specifications	~~KiXPol~~ X Band	~~JOYRAD-35~~ Ka Band	~~JOYRAD-94~~ W Band
Frequency [GHz]	9.4	35.5	94.0
Pulse Repetition Frequency [kHz]	1.2	5.0	5.3 - 12[b]
Number of FFT	1200	512	512
Number of Spectral Average	1	20	8 - 18[b]
3dB Beam Width [°]	1.3	0.6	0.5
Sensitivity at 5km [dBZ][a]	~~-14 -42~~ -10	-39	-33
Nyquist Velocity [$\pm$ms^{-1}]	9	10	4.2 - 9.7[b]
Range Resolution [m]	30.0	28.8	16 - 34.1[b]
Temporal Sampling [s]	1	2	3
Lowest clutter-free range [m]	700	400	370
Radome	Yes	No	Yes

[a] Minimum sensitivities have been derived from the reflectivity histograms shown in Fig. 8.

[b] Pulse repetition frequency, number of spectral average, Nyquist velocity and range resolution depend on the chirp definition; those values are indicated in Table 2.

Table 2. Main settings of the chirp ~~table~~ sequence used during TRIPEx for the ~~JOYRAD-94~~W Band radar. ~~(see~~ See Küchler et al. (2017) for a detailed description~~of the JOYRAD-94 chirp table)~~.

	Chirp sequence			
Attributes	1	2	3	4
Integration Time [s]	0.338	0.402	0.530	1.769
Range Interval [m]	100 - 400	400 - 1200	1200 - 3000	3000 - 12000
Range Resolution [m]	16.0	21.3	26.9	34.1
Nyquist Velocity [$\pm$ms^{-1}]	9.7	8.1	6.2	4.2
Doppler FFT	512	512	512	512
Number of Spectral Average	8	8	8	18
Chirp Repetition Frequency [kHz]	12.2	10.2	7.8	5.3

grid. At this stage, the data can be still considered raw; further processing steps that are either dependent on ~~electromagnetic~~ radar frequency or atmospheric conditions are applied to the Level 2 dataset. These processing steps include the ~~exclusion~~ detection and removal of measurements affected by ground clutter, ~~the relative calibration~~ an offset correction of the radars ~~with~~ based on independent sources, the compensation for estimated differential attenuation ~~due to~~ caused by atmospheric gases, ~~the cross-calibration among~~ adjustment of the DWRs by cross calibrations between the three radars, and the addition of data quality flags. These ~~processing~~ steps are meant to remove spurious multi-frequency signals, that are not ~~connected with cloud microphysical processes~~produced by cloud properties. The processing is performed to the best of our knowledge, however, ~~the intermediate transformations are kept within the database, allowing us~~ intermediate steps are included in the dataset in order to allow to recover the original data at any stage and ~~possibly~~ apply different processing techniques. Figure 2 illustrates the ~~work-chain~~ work chain from Level 0 to Level 2. ~~A~~ The following sections provide a detailed description of each step~~is provided in the following sections~~.

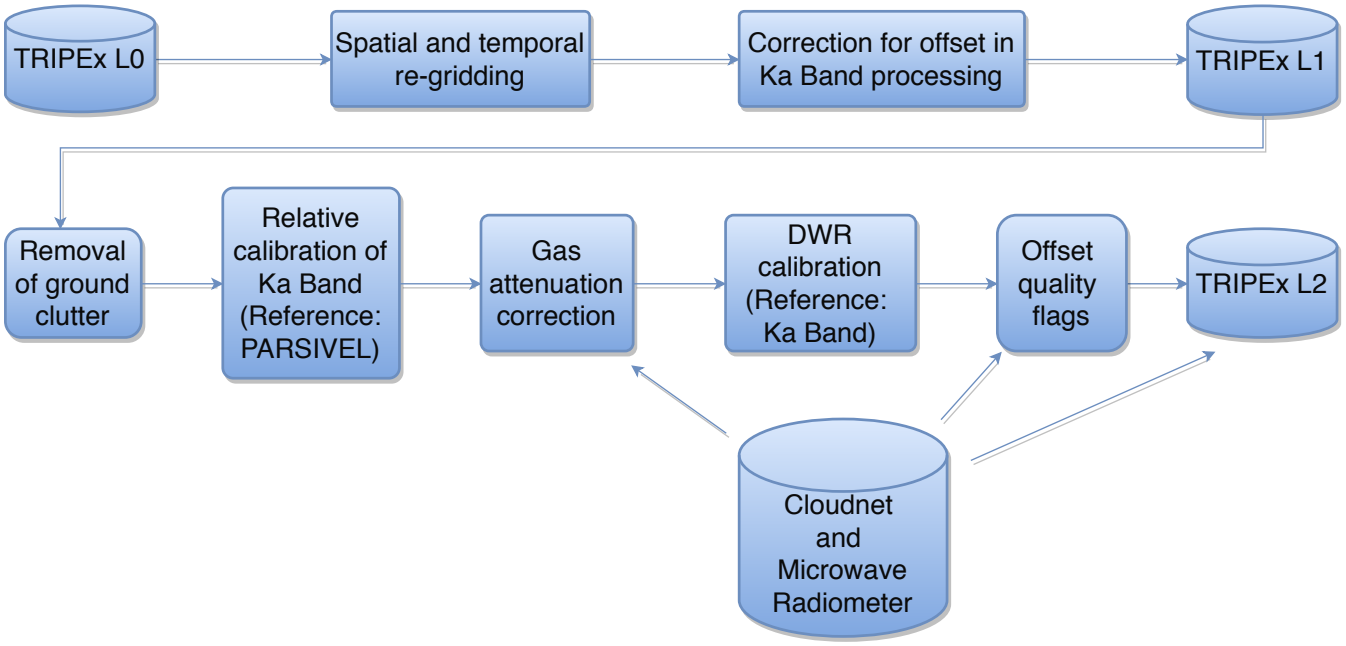

Figure 2. Flowchart of the TRIPEx data processing. The upper part describes the steps ~~applied for the~~ producing data Level 1 and the bottom part ~~describes the steps applied for the~~ those producing data Level ~~2 product which is the product used in this study.~~2.

3.1 Spatio-temporal re-gridding and offset correction

~~As shown in Table 1,~~ Since the range and temporal ~~resolution~~ resolutions of the three radars are slightly different ~~. The data are~~ (Table 1), the data is re-gridded on a common time and space ~~domain~~ resolution in order to ~~derive e.g.~~ allow for the calculation

of dual wavelength ratios ~~DWRs which is~~ (DWRs) defined for two wavelengths $\lambda 1$ ~~,~~ and $\lambda 2$ as

$$\mathrm{DWR} = \mathrm{Ze}_{\lambda 1} - \mathrm{Ze}_{\lambda 2} \quad (1)$$

~~where~~ with Ze_{λ} ~~is~~ in dBZ. ~~To this goal, we first defined a reference grid with a base~~ The reference grid has a temporal resolution of ~~of~~ 4 s and a vertical resolution of 30 m~~which is close to the original data resolution ; the reference of the new height grid is the altitude of the W-Band radar~~, which is the resolution of W Band. The data ~~values~~ are interpolated using a ~~*nearest neighbour* approach and~~ nearest-neighbour approach with the maximum data displacement ~~is~~ limited to ± 17 m in range and ± 2 s in time. ~~Using the nearest-neighbour method ensures to conserve~~ This method preserves the high resolution information of the original radar observations. ~~The reason for limiting~~ Limiting the interpolation displacement ~~is to avoid~~ avoids spurious multi-frequency features ~~,~~ that may result from non-matching radar volumes. ~~Effects of the residual volume mismatch~~ Residual volume mismatches may occur at cloud boundaries where ~~cloud heterogeneity is most prominent. For JOYRAD-35 we also applied two corrections~~ heterogeneities are largest. For Ka Band, two corrections are applied to the original ~~radar moments~~ reflectivity as suggested by the manufacturer (Matthias Bauer-Pfundstein, Metek GmbH, personal communication)~~: in order~~ . An offset of 2 dB is added to account for power loss ~~due to~~ caused by the finite receiver bandwidth~~, an offset of 2~~ ; another 3 dB ~~has been added . In addition, in order~~ offset is added to correct for ~~an issue~~ problems in the Digital Signal Processor used in older MIRA systems~~another 3 offset to the JOYRAD-35 reflectivity factors has been added. We apply these corrections to Ze~~ . These corrections are applied for processing of the Level 1 data.

3.2 ~~Evaluation of the JOYRAD-35 calibration with PARSIVEL disdrometer measurements~~Clutter removal

~~For the Level 1 processing we accounted for known~~ Following the corrections for radar offsets and ~~re-gridded the data onto a common time-height grid. In the following steps, we calibrate the three radars relatively to each other and estimate the quality based on the applied corrections. Our relative calibration approach follows the previous triple-frequency study by Kneifel et al. (2015)). First, radar~~ re-gridding, the first step in the Level 2 processing is the removal of the range gates affected by ground clutter~~are detected and removed from the database according to the height thresholds listed~~ . Considering the different radar installation locations (roof mount or ground surface) and antenna patterns, the clutter contamination affects each radar data differently. The thresholds for the lowest usable range gates are determined empirically and are reported in Table 1. ~~For the relative calibration we take JOYRAD-35 as reference, because of its better sensitivity level compared to KiXPol up to high elevations and its lower signal attenuation compared to W-Band. Moreover, JOYRAD-35 is the only system not~~

3.3 Evaluation of the Ka Band calibration with PARSIVEL disdrometer measurements

The three radars have been individually calibrated by their respective manufacturers, however, radar components might experience drifts over time which can lead to biases of several dB. The JOYCE site is equipped with a ~~radome which might collect raindrops on its surface and cause additional attenuation. We also expect that signal attenuation due to antenna wetness on JOYRAD-35 to be lower because of the periodic antenna tilts during RHI scans.~~

In order to evaluate the quality of the JOYRAD-35 calibration, we compared the reflectivities measured at 500 - 600 m with those derived from drop size distributions PARSIVEL optical disdrometer (Löffler-Mang and Joss, 2000) which provides the drop size distribution (DSD) observed by a co-located Parsivel optical disdrometer (Löffler-Mang and Joss (2000)) during three light rainfall events. The with a temporal resolution of one minute. For rainfall events, the DSD can be used to calculate the associated radar reflectivity factor. In this study, the scattering properties of raindrops have been computed are calculated using the T-matrix approach (Leinonen, 2014) assuming with a drop shape model that follows Thurai et al. (2007) and assuming drop canting angles that follow a Gaussian distribution of canting angles with zero mean and 7° standard deviation (Huang et al., 2008). The Parsivel was unfortunately not functioning during the TRIPEx campaign itself, hence we did the comparison for two cases before and one case after the campaign. These precipitation events lasted for several hours and provided thus meaningful statistics. The frequency distributions of the reflectivities measured by JOYRAD-35 and calculated using T-matrix are shown in Figure 3. While the overall shapes of the two histograms are very similar, the mean values from JOYRAD-35 are in every case approximately 4 Unfortunately, the lowest usable radar range gates are 500 - 600 m above the PARSIVEL, thus we have to assume a constant DSD over this altitude range in order to compare with the radar reflectivities. Time lags and wind shear effects raises further problems to the direct comparisons between radar measured Ze and the one calculated with PARSIVEL. For this reason, we compare only the statistical distribution of reflectivities at the lowest range gates measured over several hours with the corresponding distribution calculated at the ground level. Of course, systematic differences caused by rain evaporation, drop breakup, or drop growth due to accretion towards the ground may affect such comparisons. However, the changes in the Ze profile are very close to the ones predicted by attenuation and constant DSD from three light rainfall cases. The reflectivity distributions from PARSIVEL and Ka Band (Figure 3) of those periods are very similar but differ by approximately 3.6 dB lower than the those derived from the T-matrix model. This persistency suggests a bias due to radar miscalibration, which we corrected accordingly in the JOYRAD-35 dataset being aware of the caveats of radar-disdrometer comparisonswith Ka Band having the lower reflectivities. For these comparisons, periods before and after the TRIPEx campaign had to be used, because PARSIVEL had a hardware failure during the campaign. The similarity of the the results gives us indication that this method is reliable, however, a large number of cases is still needed in other to draw a final conclusion about this method. Unfortunately, only Ka Band was available because the other two radars were not measuring during the selected rainfall events.

3.4 Correction for atmospheric gas attenuation

Hydrometeors and atmospheric gases cause considerable attenuation at cloud radar frequencies. We correct The reflectivities from X, Ka, and W Band are corrected for estimated attenuation due to atmospheric gases (Fig. 2) by means of the Passive and Active Microwave TRAnsfer model (PAMTRA) (Maahn et al., 2015). PAMTRA calculates specific attenuation due to molecular nitrogen, oxygen and water vapor based on the gas absorption model from Rosenkranz (1998)Rosenkranz (1993, 1998, 1999). Input parameters are the vertical profiles of atmospheric temperature, pressure and humidity provided by the CloudNet product products (Illingworth et al., 2007), which is are generated operationally at the JOYCE-CF site. The two-way path integrated attenuation (PIA) at the radar range gates is derived from the specific attenuation integrated along the vertical. Table 3 lists the minimum and maximum two way two-way attenuation values at ≈ 12 km (height of the maximum range gate in Level 2 data)

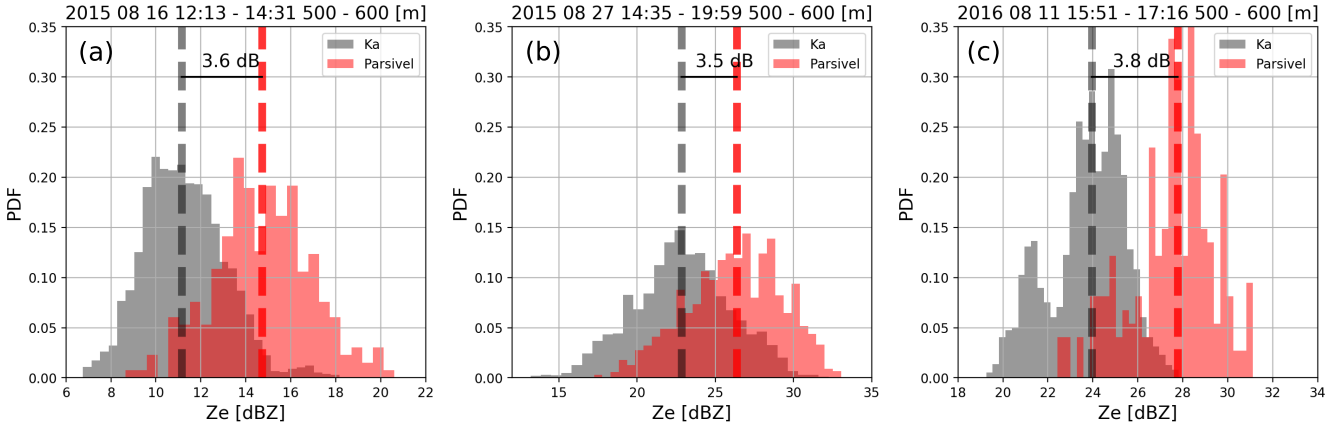

Figure 3. Histograms of radar reflectivities from ~~JOYRAD-35~~ Ka Band (gray) and results from T-matrix ~~calculation~~ calculations with the rain drop size distribution provided by ~~Parsivel~~ PARSIVEL (red) for three long-lasting stratiform rain cases before and after the TRIPEx campaign (16 August 2015 (~~A~~a), 27 August 2015 (~~B~~b), 11 August 2016 (~~C~~c)). ~~JOYRAD-35~~ Ka Band reflectivities are taken from the lowest clutter-free range gates between 500 and 600 m. The vertical dashed line indicates the median of the distribution; the offset is calculated as the difference between ~~JOYRAD-35~~ Ka Band and T-matrix results.

for the three radars during the entire campaign. The highest attenuation of ≈ 2.6 dB ~~- mainly caused by water vapor -~~ occurs at 94 GHz ~~. The lowest~~ and is mainly caused by water vapour. Conversely, the 9.4 GHz maximum attenuation of ≈ 0.1 dB is ~~found for 9.4 , which~~ the lowest among the three radars and it is mainly produced by oxygen continuum absorption. At 35.5 GHz, ~~where~~ attenuation is governed by both oxygen and water vapour~~, the maximum attenation~~ . The maximum attenuation value found at this frequency is ≈ 0.7 dB~~and thus between those found at 9.4 and 94~~ .

Table 3. Calculated minimum and maximum two-way path integrated attenuation (PIA) at a height of ≈ 12 km for ~~X~~ X, ~~Ka~~ Ka, and ~~W-Band~~ W Band during TRIPEx.

Frequency [GHz]	Minimum Attenuation [dB]	Maximum Attenuation [dB]
9.4	0.077	0.104
35.5	0.365	0.728
94	0.650	2.675

3.5 ~~Inter radar~~ DWR calibration and generation of quality flags

Spurious ~~non-physical~~ multi-frequency signals can arise from attenuation effects due to particulate atmospheric components (e.g. ~~,~~ liquid water, melting layer, snow), but also from instrument specific effects such as a wet radome, snow on the antenna, and remaining relative offsets due to radar mis-calibration. ~~The last stepin the Level 2 processing is an estimate of the relative offset among the three radars~~With this processing step, the reflectivity measurements are adjusted in order to take into account

the cumulative effects of the aforementioned bias mechanisms at the top of the clouds. By doing so, the effects of the cloud microphysical processes on the DWR signals are recovered.

Ka Band is used as reference because of its better sensitivity level and larger dynamic range compared to the other radars (up to high altitudes) and its lower signal attenuation compared to W Band. Moreover, Ka Band is the only system not equipped with a radome which might collect raindrops on its surface and cause additional attenuation. The signal attenuation due to antenna wetness on Ka Band is expected to be lower compared to other radars' radome attenuation because of the periodic antenna tilts during RHI scans (every 30 minutes). The processing is complemented by ~~a series~~ the generation of quality flags categorized as errors and warnings. Error flags mark data ~~affected by a poor quality of~~ of poor quality based on the applied correction procedure, ~~and the~~ while warnings indicate the detection of potential sources of ~~inter-radar offsets that are not~~ DWR offsets that have not been accounted for in the procedures described below. An additional error flag is raised if spurious multi-frequency signals due to radar volume mismatch are suspected. A list of all the quality flags (both errors and warnings) is provided in Table 4.

~~Following the methodologies applied by Kneifel et al. (2015) and Hogan et al. (2000), we assume that~~ The small ice particles in the upper parts of ~~the cloud~~ clouds are mostly Rayleigh scatterers ~~; thus~~(Kneifel et al., 2015; Hogan et al., 2000) thus, their reflectivities should not be frequency dependent (Matrosov, 1993). ~~We estimate the~~ The reflectivity range, ~~for which we can make this assumption,~~ at which the Rayleigh approximation can be assumed, is estimated by investigating the behaviour of the ~~respective~~ observed DWRs as function of Ze_{Ka}. ~~The uncorected~~ Within the Rayleigh regime, the measured DWRs are expected to remain constant ~~within the Rayleigh regime and~~ at a value that accounts for all the integrated differential attenuation and radar miscalibration effects. As the ice particles grow larger, the DWRs start to deviate from that ~~value when particles in the resepective radar volumes enter the Mie regime first for~~ constant value and this deviation affects the higher-frequency ~~radar. Separate reflectivity thresholds are needed~~ radars first. Because of that, the Rayleigh data has been isolated by means of two different reflectivity thresholds for X and ~~W-Band since the transition into Mie scattering is expected to happen at larger Ze for X-Band than for W-Band~~W Band radars. In addition, the sensitivity of ~~the X-Band~~ X Band is much lower~~and thuswe need to accept a larger reflectivity threshold~~ ; thus, a higher reflectivity threshold is accepted for the offset estimate between X and ~~Ka-Band~~Ka Band compared to Ka and W Band. For the ~~relative offset estimate of the W-band radar~~determination of the relative offset for W Band, we found an optimal range of $-30 < Ze_{Ka} < -10$ dBZ, ~~while for the X-band radar the range of~~ and $-20 < Ze_{Ka} < -5$ dBZ ~~was used~~for X Band. In order to safely exclude partially melted particles, ~~we only use~~ only reflectivities from at least 1 km above the 0 °C isotherm ~~.~~ are used.

The relative offset correction is estimated for each ~~time instant based on the data of~~ measuring time from the data inside a moving time window of 15 minutes~~centered over that time instant and restricted to reflectivity pairs, which obey the previously stated conditions~~. The selected data are restricted to the reflectivity pairs which are within threshold values defined above. The mean value of the DWR computed for these reflectivity pairs constitutes the ~~relative inter radar~~ DWR offset. The quality of ~~the relative offset correction~~ this offset estimation strongly depends on the quality and quantity of the reflectivity data included in the ~~moving time window. A large number of~~ average. Empirical analysis showed that at least 300 data points spanning ~~through many reflectivity values within the Rayleigh regime is~~ a wide reflectivity range are required in order to ~~reliably estimate the~~

relative offset between the radars. Estimates from less than 300 valid reflectivity pairs might contain large have acceptable sampling errors. Moreover, in regions close to cloud edges or for Ze The data that present a smaller sampling statistics are marked with an error flag.

Whenever cloud edges are included in the sampling volume and/or when the measured Ze is close to the sensitivity limits of the radars, the statistical correlation of the two reflectivities instruments, the correlation between the reflectivities of two radars might strongly deteriorate. Thus, we flag time periods characterized by reflectivity correlations below In order to help the user identify these potential sources of errors, the data profiles presenting a correlation lower than 0.7 or number of valid reflectivity pairs below 300 as unreliable. The two criteria for the offset quality are stored separately as error quality flags (see Table 4). are marked with an additional error flag.

Despite the matching procedure of the different frequency radar volumes (section 3.1), mismatches are unavoidable due to the horizontal distances between the radars (Figure 1), the different radar range resolutions and beam widths (Table 1). At cloud edges and close to the melting layer, where the largest spatial cloud inhomogeneities are expected, the effects of the remaining radar volume mismatches will be maximized. The temporal DWR variability during 2-minutes moving windows is used as an indicator for potential volume mismatch; cloud regions with variances above 2 dB^2 are flagged accordingly.

Table 4. Quality flags included in the data Level 2 product (bit-coded in a 16-bit integer value). The flags indicate the reliability of the data and in particular relation to the applicability quality of the relative offset estimate for X-Ka and W-Ka band Band reflectivities. Note that offsets are not calculated, when the number of reflectivity pairs is below 300.

	Bits	Criteria
Warning	0-5	Reserved for future warning flags
	6	LWP >200 gm^{-2}
	7	Rain detected by CloudNet
Errors	8-12	Reserved for future error flags
	13	Variance in time of DWR >2 dB^2
	14	Correlation of data points is poor (<0.7)
	15	Number of valid measurements <300

The described correction adjustment technique accounts for all processes , which that affect relative offsets of the radars in the upper , frozen part including and frozen part of clouds. These processes include possible frequency-dependent attenuation effects occurring at lower levelsbesides radar miscalibration from lower levels, radar mis-calibration and radome/antenna attenuation. Since the estimated correction is , however, applied to the entire profileinevitably an overcompensation will , inevitably over-compensations might occur in the lowerrainy part. Thus, the data should only be used for , possibly rainy parts of clouds. This limitation is necessary in order to increase the quality of the data in the ice part of the cloud, for which microwave attenuation can be considered negligible, and which was clouds, which is the main focus of the campaign. Differential attenuation in the ice part of the cloud can, however, be generated by super-cooled liquid drops; thus the subsequent analysis of the DWR signal in that part of the cloud might be affected by this error. Especially area of the presented study.

The lack of information about vertical hydrometeor distribution prevents reliable reflectivity corrections by differential attenuation. As a consequence of the presented DWR calibration and the fact that hydrometeor attenuation is hitting the higher frequencies more, the computed DWRs are expected to be increasingly underestimated towards the ground. A refined correction should be applied for rain and melting layer studies~~or when information about~~. Possible sources of of information about the amount and position of super-cooled liquid water ~~is available, e.g. form lidar or~~ could be collocated lidar or analysis of radar Doppler spectra ~~, a refined correction can and should be applied. Additional warning flags indicate periods with larger liquid water path~~ measurements. Those data are available at JOYCE-CF but they are not included in the current dataset. However, an additional warning flag indicates periods with large liquid water paths derived from the ~~nearby microwave radiometer~~or collocated microwave radiometer. Lastly, the occurrence of rainfall and/or a melting layer from the CloudNet classification and indicated by the precipitation gauge ~~, and are summarized in Table 4~~is marked with an additional warning flag (Table 4).

~~Despite the technically optimal match of the different frequency radar volumes, mismatches are unavoidable due to the horizontal distances between the radars (Figure 1), the different radar range resolutions and beam widths (Table 1). At cloud edges and close to the melting layer , where the largest spatial cloud inhomogeneities can be expected, the impact of the remaining radar volume mismatch on the DWRs will be maximum. We used the temporal variability of the DWRs estimated from 2-minutes moving windows as an indicator for potential volume mismatch. Cloud regions with variances above 2 dB^2 are flagged. Filtering of these data reduces the scatter of data in the triple-frequency space, but also might remove interesting data from regions with strong signal gradients~~

4 Overview of the dataset

The Level 2 of the TRIPEx dataset contains radar moments, polarimetric variables, integrated attenuation and atmospheric state variables. The polarimetric variables are included as they are provided by the radar software and no additional processing or quality check is applied to them. Z_{dr}, ϕ_{dp} and ρ_{hv} from X Band might be a useful additional source of information for melting layer studies (Zrnić et al., 1994; Baldini and Gorgucci, 2006). We are not confident about the quality of K_{dp} provided by the X Band software, and therefore, this variable is not included in the dataset but can be calculated by the user. Table 5 lists all variables available in Level 2.

The dataset contains 47 days of measurements. For each day, table 6 lists the atmospheric conditions such as temperature at 2 m (T 2m), rain rate (RR), accumulated rain (AR), liquid water path (LWP), and integrated water vapor (IWV). The duration of four empirically classified predominant types of cloud and precipitation is provided for each day 6. The two most frequent cloud types are ice clouds (IC) with 377 hours and shallow mixed-phase clouds with 222 hours of observations. Stratiform rainfall (SR) occurred during 137 h while rain showers (SR) were only observed during 47 hours. The average rain rate (RR) for all rainy periods over the whole period (mean rain intensity) is 0.078 mmh^{-1} with a maximum instantaneous RR of 8.07 mmh^{-1}. DWR signatures and radar Doppler information suggest that the ice part of clouds is dominated by depositional growth and aggregation. Riming seems to occur only during a few short events. Although the dataset spans the main winter

Table 5. Variables available in the TRIPEx dataset Level 2.

Radar variables	X Band	Ka Band	W Band
Reflectivity [dBZ]	x	x	x
Mean Doppler velocity [ms^{-1}]	x	x	x
Spectral width [ms^{-1}]	x	x	x
Differential reflectivity [dB]	x	—	—
Differential propagation phase shift [°]	x	—	—
Co-polar correlation coefficient	x	—	—
Linear depolarization ratio [dB]	—	x	—
way path integrated attenuation [dB]	x	x	x

Atmospheric variables	CloudNet
Air temperature [°C]	x
Air pressure [Pa]	x
Relative humidity [%]	x

season, no snowfall was recorded at the surface. In the following, we will demonstrate the effect of applying data quality flags and discuss remaining limitations as well as the effects of the different radar sensitivities.

4.0.1 ~~Example of data filtering based on quality flags~~

4.1 Effects of data filtering based on quality flags

The ~~effect of the different quality flag and additional filtering approaches~~ effects of data filtering on DWR_{XKa} and DWR_{KaW} is demonstrated for ~~the~~ clouds observed on 20.11.2015 in ~~Figure~~ Figures 4 and 5. ~~For a better visualization~~ In order to give a better visual impression of these effects, the filtering steps are applied ~~cumulatively. In panels A-C~~ sequentially and cumulatively. Panels a-c of Figure 4 show the unfiltered Level 2 data~~are shown~~. The time-height plot (panels ~~A and B~~ a and b in Figure 4) reveal a stratiform cloud passing over the site from 01:00 to 17:00 UTC followed by a series of low-level, shallow, most likely mixed-phase clouds. The short periodic gaps ~~are due to~~ result from interruptions of zenith observations ~~by RHI scans of JOYRAD-35~~caused by range-height indicator (RHI) scans of Ka Band, and the large gap in DWR_{KaW} between 09:00 and 10:00 UTC ~~results from missing JOYRAD-94~~ is caused from missing W Band observations. The -15 °C isotherm (dashed line in the time-height plots) ~~marks a clear vertical separation between the DWRs , which remain~~ separates DWRs around 0 dB for temperatures below -15 °C ~~and rapidly increase~~ from rapid increases with reflectivity for higher temperatures.

Panel ~~C~~ c in Figure 4 ~~is a 2D~~ displays a scatter density plot of DWR_{XKa} versus DWR_{KaW} (hereafter called triple-frequency plot). The position ~~of the measured data~~ in the triple-frequency plot is mainly driven by the respective hydrometeors bulk density ρ and ~~the~~ their mean volume diameter~~of the particle size distribution~~ D_0~~(see Kneifel et al. (2015) for more detail). This~~ (Kneifel et al., 2015). This plot allows to discriminate between the two ~~snow~~ processes: rimed particles follow the flat

Table 6. Characterization of the atmospheric conditions and estimated duration of cloud/precipitation events during TRIPEx. T 2m is the air temperature at 2 m from a nearby weather station. RR and AR are the rain rate and the accumulated rain measured by a Pluvio disdrometer; mean RR is calculated using all RR values larger than 0 mmh^{-1}. Liquid water path (LWP) and integrated water vapor (IWV) are derived from the collocated 14-channel microwave radiometer; mean LWP is calculated using all LWP values larger than 0.03 kgm^{-1} in order to exclude clear-sky periods. The columns with IC, SR, RS and MP indicate the approximate duration in hours of non-precipitating ice clouds, stratiform rain, rain showers, and shallow mixed-phase clouds, respectively.

date	T 2m [C]	RR [mmh^{-1}]	AR	LWP [kgm^{-2}]	IWV [kgm^{-2}]	IC	SR	RS	MP
yyyy.mm.dd	max / min	max / mean	[mm]	max / mean	max / mean	[h]	[h]	[h]	[h]
2015.11.11	12.85 / 11.13	0.00 / 0.00	0.00	0.42 / 0.10	25.76 / 17.50	9	0	0	24
2015.11.12	12.81 / 10.25	0.00 / 0.00	0.00	0.29 / 0.07	20.58 / 17.34	18	0	0	18
2015.11.13	13.89 / 7.52	0.66 / 0.27	0.59	1.61 / 0.15	23.72 / 15.82	13	0	8	6
2015.11.14	10.86 / 6.46	0.33 / 0.12	0.79	0.38 / 0.10	19.34 / 12.23	12	10	0	0
2015.11.15	15.99 / 10.15	0.15 / 0.05	0.08	0.63 / 0.11	28.27 / 20.87	11	0	0	21
2015.11.16	13.74 / 11.45	2.16 / 0.40	2.16	2.64 / 0.15	28.65 / 18.99	4	4	3	12
2015.11.17	15.83 / 11.94	5.97 / 0.82	8.31	1.68 / 0.16	29.39 / 19.23	10	0	10	0
2015.11.18	14.60 / 11.41	8.07 / 1.88	4.40	1.65 / 0.13	27.71 / 15.02	6	0	0	14
2015.11.19	11.76 / 8.41	5.64 / 1.16	12.82	1.70 / 0.20	23.51 / 17.22	13	12	2	0
2015.11.20	9.45 / 4.87	1.08 / 0.27	1.02	0.98 / 0.13	19.02 / 13.63	10	3	0	6
2015.11.21	5.66 / 2.17	0.30 / 0.11	0.23	1.38 / 0.12	15.38 / 8.820	4	0	7	6
2015.11.22	5.33 / -0.09	7.35 / 3.80	2.54	0.84 / 0.07	11.11 / 8.17	4	0	5	2
2015.11.23	5.32 / -0.42	0.00 / 0.00	0.00	0.52 / 0.08	9.81 / 7.83	7	0	0	2
2015.11.24	4.51 / 0.19	1.26 / 0.28	1.30	0.53 / 0.17	16.71 / 12.57	10	12	0	0
2015.12.03	11.90 / 6.63	0.00 / 0.00	0.00	0.03 / 0.03	15.38 / 13.59	10	0	0	5
2015.12.04	11.39 / 5.87	2.67 / 0.56	3.38	0.57 / 0.21	24.09 / 10.98	4	4	0	2
2015.12.05	10.20 / 4.47	0.00 / 0.00	0.00	—	9.77 / 7.19	16	0	0	0
2015.12.06	12.86 / 3.34	0.00 / 0.00	0.00	0.39 / 0.11	24.14 / 15.63	2	0	0	12
2015.12.07	14.53 / 8.74	0.03 / 0.03	0.00	0.51 / 0.13	24.31 / 18.81	9	0	4	8
2015.12.08	14.66 / 7.92	2.67 / 0.84	4.06	0.84 / 0.18	23.01 / 14.67	2	5	0	0
2015.12.09	9.34 / 2.20	0.06 / 0.03	0.04	0.48 / 0.08	18.89 / 8.96	0	4	0	1
2015.12.10	8.81 / 0.77	0.00 / 0.00	0.00	—	11.86 / 6.49	7	0	0	0
2015.12.11	8.61 / 4.77	2.16 / 0.57	9.34	0.41 / 0.17	19.81 / 16.18	2	20	0	0
2015.12.12	10.42 / 4.7	0.03 / 0.03	0.02	0.36 / 0.09	21.10 / 15.73	16	0	0	0

continue next page

date	T 2m [C]	RR [mmh^{-1}]	AR	LWP [kgm^{-2}]	IWV [kgm^{-2}]	IC	SR	RS	MP
yyyy.mm.dd	max / min	max / mean	[mm]	max / mean	max / mean	[h]	[h]	[h]	[h]
2015.12.13	10.08 / 6.18	3.09 / 0.37	5.50	1.07 / 0.38	22.73 / 19.10	7	0	0	8
2015.12.14	9.24 / 3.36	0.03 / 0.03	0.02	0.17 / 0.08	16.00 / 12.95	6	0	0	0
2015.12.15	10.3 / 3.89	0.39 / 0.16	0.16	0.57 / 0.15	23.55 / 17.51	12	2	3	0
2015.12.16	13.04 / 8.90	2.49 / 0.39	6.02	—	—	0	10	0	7
2015.12.17	16.28 / 12.53	3.60 / 0.48	0.72	1.12 / 0.15	25.61 / 20.01	8	0	0	6
2015.12.18	13.11 / 8.74	0.27 / 0.17	0.08	0.71 / 0.12	26.64 / 16.45	10	0	1	2
2015.12.19	13.21 / 9.93	0.00 / 0.00	0.00	0.27 / 0.09	25.11 / 22.70	8	0	0	0
2015.12.20	13.22 / 11.31	0.00 / 0.00	0.00	0.44 / 0.10	23.15 / 20.99	22	1	0	0
2015.12.21	12.17 / 9.52	0.72 / 0.18	0.45	0.84 / 0.13	23.52 / 14.49	3	3	1	6
2015.12.22	14.75 / 10.41	2.19 / 0.41	1.45	0.61 / 0.08	26.53 / 22.00	16	2	0	8
2015.12.23	13.00 / 4.38	0.45 / 0.21	0.42	0.23 / 0.07	14.21 / 11.24	4	0	0	8
2015.12.24	14.51 / 4.38	5.34 / 0.68	1.82	1.14 / 0.11	22.91 / 15.40	6	0	1	3
2015.12.25	13.35 / 7.78	3.27 / 0.81	4.72	0.60 / 0.13	24.76 / 18.32	15	8	0	4
2015.12.26	15.78 / 7.17	0.00 / 0.00	0.00	0.20 / 0.08	22.51 / 17.55	4	0	0	4
2015.12.27	14.40 / 6.13	0.00 / 0.00	0.00	—	18.71 / 14.20	12	0	0	0
2015.12.28	11.07 / 5.12	0.00 / 0.00	0.00	—	9.56 / 8.57	11	0	0	0
2015.12.29	11.87 / 4.35	0.00 / 0.00	0.00	0.34 / 0.08	19.78 / 13.80	2	3	0	0
2015.12.30	9.40 / 3.77	0.00 / 0.00	0.00	0.05 / 0.04	17.80 / 10.93	3	0	0	0
2015.12.31	10.31 / 3.53	0.69 / 0.20	0.47	1.01 / 0.22	24.39 / 11.82	4	3	2	0
2016.01.01	8.45 / 3.46	0.30 / 0.13	0.10	0.83 / 0.13	15.42 / 9.85	13	0	0	6
2016.01.02	5.94 / 4.11	2.88 / 0.72	4.69	0.42 / 0.14	17.80 / 12.89	6	7	0	8
2016.01.03	8.29 / 4.84	1.86 / 0.44	2.95	0.93 / 0.23	19.85 / 14.45	6	14	0	4
2016.01.04	7.74 / 3.66	3.57 / 0.81	7.06	—	—	0	10	0	9
Total						377	137	47	222

curve (low DWR_{XKa}) due to their higher density, while aggregated particles give rise to a ~~bending up~~ bending-up signature (increase in DWR_{XKa} while DWR_{KaW} saturates or even decreases) due to their lower density, which is nicely shown in Figure 4, Panel ~~C~~c.

~~Apparently, a~~ A large number of points in Panel ~~C~~c, Figure 4 populate ~~in~~ areas which are unrealistic from a microphysical point, such as negative DWRs. Some of those originate from time periods when the offset ~~can not be calculated~~ cannot be calculated properly or when the correlation between the three radars is poor. Panels ~~D and E~~ d and e in Figure 4 show the results after removing ~~these data~~ those points (bits 14 and 15 in the quality flag, see Table 4), an effect best visible between 17:00 and 20:00 for DWR_{KaW} and between 17:00 and 23:00 for DWR_{XKa}. ~~This leads to~~ The triple-frequency plot (Panel

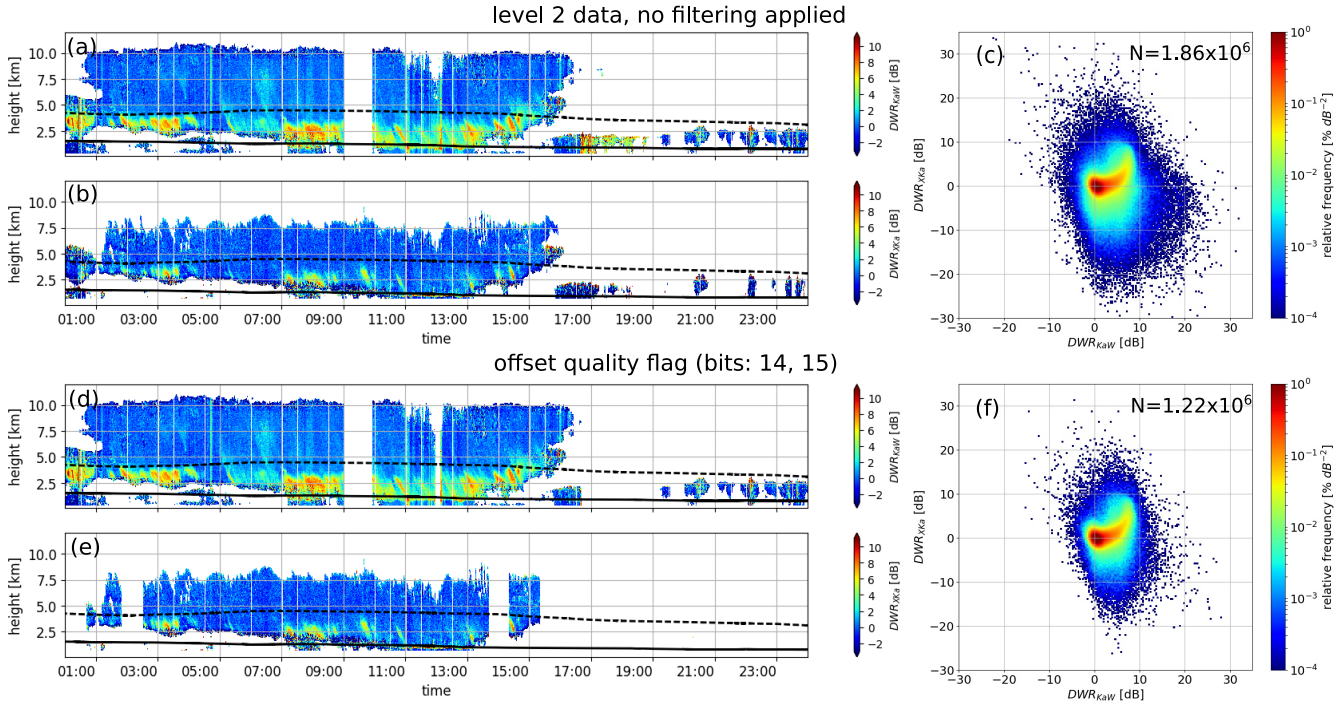

Figure 4. Time-height plots of DWR_{KaW} (Panel ~~A~~a) and DWR_{XKa} (Panel ~~B~~b) using the Level 2 data of 20.11.2015 without applying any filtering. The continuous line and dashed line are the ~~isotherm of~~ 0 and -15 °C ~~, respectively~~ isotherms (provided by the CloudNet products), respectively. The triple-frequency signatures for the ice part of the clouds are shown on the right (Panel ~~C~~c). Panels ~~D-F~~ d-f show the remaining data after applying the offset quality flags and ~~restricted~~ the restriction to data pairs with sufficient correlation. N in Panels ~~C~~ c and ~~F~~ f indicates the respective number of data pairs in the ice part of the clouds. Note the log-scale on the colorbars in c and f.

f in Figure 4) shows a strong reduction of outliers~~from the aggregation signature in the~~ , when compared to the unfiltered triple-frequency ~~space (Panel F~~ plot (Panel c in Figure 4).

Despite the data filtering described in the previous paragraph, the scatter around the main signature is still large. Panels ~~A and B~~ a and b in Figure 5 show the time-height plots after removing observations flagged with the DWR 2-minute temporal variance flag (bit 13 in the quality flag, see Table 4). This filtering step removes most of the outliers from the aggregation signature in the triple-frequency plot (~~panel C~~ Panel c in Figure 5). It is worth noting that the removal of such data reduces the scatter in the triple-frequency space, but might also remove interesting measurements from regions with strong reflectivity gradients. An additional 3-minutes running-window averaging of the reflectivities ~~(panels D and E~~ keeps the most stable signatures (Panels d and e in Figure 5)~~further removes the scatterand even more~~ , further removes scatter, and thus accentuates the aggregation signature in ~~the~~ triple-frequency ~~space (panel F~~ plot (Panel f in Figure 5). The averaged reflectivities, calculated in this procedure, are not included in the TRIPEx dataset because it would not be possible to retrieve the original data~~from the mean values~~. The last two quality flags (bits 7 and 6, see Table 4) mark ~~the~~ data acquired during rainfall ~~periods via~~ according

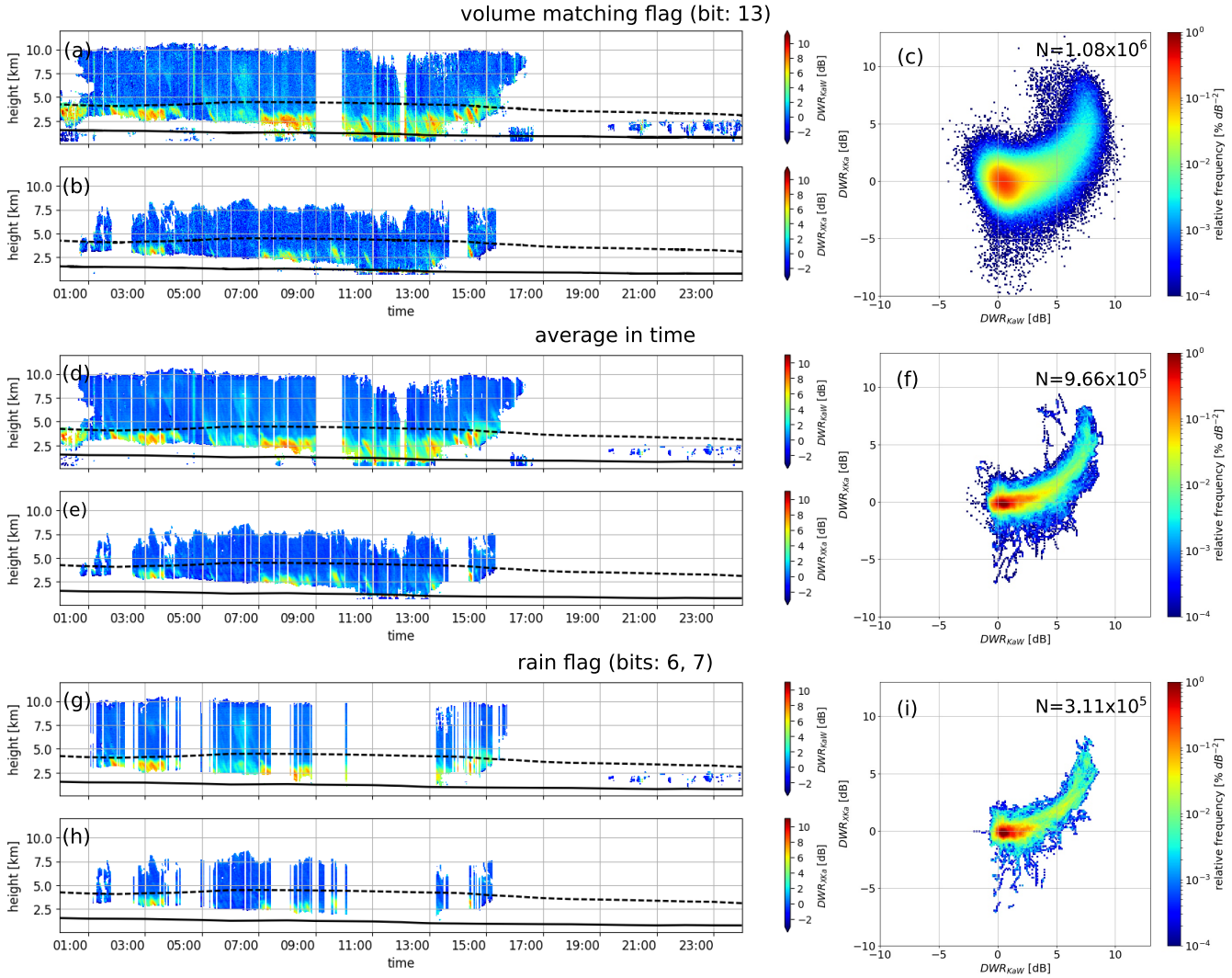

Figure 5. Same as Figure 4, but here the effects of cumulative data filtering subject to different quality flags and averaging is illustrated. Panels ~~A-C~~ a-c display the effect of filtering based on the DWR variance in time, which removes areas potentially affected by ~~bad~~ poor radar volume matching. The effect of an additional temporal averaging over 3 minutes is shown in Panels ~~E-F~~e-f. The effect of the removal of time periods with rain as identified by CloudNet or large liquid water ~~pathes~~ paths measured by the nearby microwave radiometer are displayed in Panels ~~G-I~~g-i. Note the log-scale on the colorbars in c, f and i.

to the CloudNet product and times ~~characterized by~~ with total liquid water path ~~above~~ larger than 200 gm^{-2} ~~measured~~ as estimated by the microwave radiometer. ~~Filtering according to these flags quite~~ The latter filtering significantly reduces the amount of ~~data (panel G and H~~ usable data (Panel g and h in Figure 5), but ~~the aggregation signature clearly remains visible (panel I in Figure 5).~~

4.2 ~~Radar sensitivity~~

~~The distribution of reflectivity values measured by the three radars during the entire campaign filtered with the error flags (bits 13, 14 and 15 in Table 4) and stratified by height above the site, is shown in Figure 8. As already mentioned, JOYRAD-35 and JOYRAD-94 show higher sensitivities compared to KiXPol up to high altitudes. JOYRAD-35 (Panel B in Figure 6) exhibits the largest dynamic range compared to JOYRAD-94 and KiXPol (Panels A and B in Figure 6). The step-wise shape of the lowest altitude reflectivities from JOYRAD-94 is caused by different chirp settings (Table 2). A polynomial fit to the minimum retrieved linear reflectivities (Ze_{lin} in units of) as function of altitude z (units of),~~

$$Ze_{lin}(z) = a \cdot z^b$$

~~results for KiXPol and JOYRAD-35 in the expected nearly quadratic decrease with range (Table 6). The slower decrease (smaller exponent)for JOYRAD-94 results from the altitude-dependent sensitivity associated with the different chirp settings.~~

~~The melting layer was mostly observed at altitudes between 1 and 2 km which caused the kinks in the reflectivity distributions and their extremes in the KiXPol reflectivites. Although the KiXPol sensitivity did not allow to monitor the ice clouds above 7 km with reflectivities below -10 dBz, dual-wavelength studies of these clouds are still possible with the JOYRAD-94 and JOYRAD-35 included in the Level 2 data. Ice aggregation and riming processes however, which are the most relevant for triple-frequency studies, usually occur at lower levels and larger reflectivities where all three radars provide sufficient sensitivity~~preserves the main aggregation signature surprisingly well (Panel i in Figure 5).

~~Histograms of reflectivities from the entire TRIPEx campaign Level 2 data for each radar. The red curve is the profile of the minimum retrieved reflectivity (Eq. 2). Panels A, B and C show the histograms for KiXPol, JOYRAD-35 and JOYRAD-94, respectively; all error flags (see Tab. 4) were applied to filter the data.~~

~~Coefficients a and b for the sensitivity fit (Eq. 2) obtained for KiXPol, JOYRAD-35 and JOYRAD-94. The coefficients were calculated using the Level 2 dataset applying error flags (see Table 4). a b KiXPol $6.25 \cdot 10^{-10}$ 2.19 JOYRAD-35 $3.41 \cdot 10^{-12}$ 2.04 JOYRAD-94 $8.36 \cdot 10^{-10}$ 1.53~~

4.2 Limitations of the current dataset

Despite the ~~processing steps to filter errors in the TRIPEx dataset~~ filtering steps discussed in Section 3.5, some limitations remain~~, which we discuss in this section in more detail. We identified~~ . As an example, on 23.11.2015 between 16:00 and 23:00 UTC ~~enhanced~~ we observe enhanced values of Ze_X (-20 up to 10 dBZ) ~~in the KiXPol observations~~ (Figure 6, Panel ~~A~~a), while ~~JOYRAD-35 (Ze_{Ka}) and Joyrad-95 (Ze_W) show no significant reflectivities~~Ze_{Ka} and Ze_W remain very low. The mean

Doppler velocity of that structure is very small (MDV between 0 and 0.5 ms^{-1}) ~~as observed by KiXPol slowly descends~~ and is associated with strongly enhanced LDR from ~~JOYRAD-35~~ Ka Band (Figure 6, Panel ~~B)and large Z_{dr}~~ b). Large Z_{dr} values are observed by the near-by ~~scanning polarimetric X-band radar (JuXPol)~~weather polarimetric X Band radars JuXPol and BoXPol (see Diederich et al. (2015) for a detailed characterization of the radars), that were performing RHI scans over the TRIPEx site at that time. The most likely explanation based on the polarimetric signature and the fall velocity are fall streaks of chaff ~~, and therefore, these periods should be avoided~~ deployed by military aircraft during a training session. We recommend to avoid this period for cloud microphysical studies. ~~Also the scanning polarimetric X-Band radars (JuxPOL and BoXPOL) revealed very large ZDR values during that period (not shown).~~

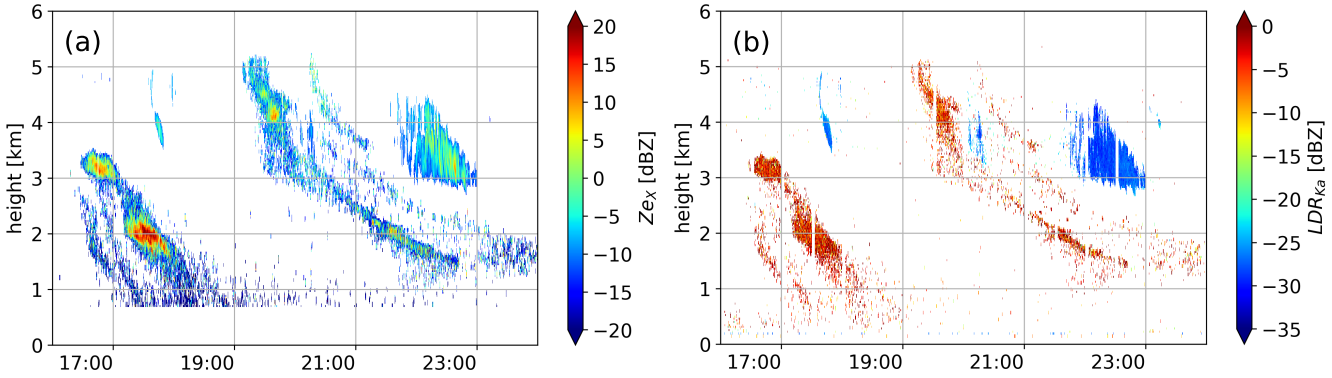

Figure 6. Time-height plots of the Ze_X and LDR_{Ka} of 23.11.2015 between 16:00 and 23:59. The region where the LDR is ≈ -5 dB is most probably a results of chaff. The ~~JOYRAD-35~~ Ka Band software applies a filtering for non-meteorological targets which removes most of the chaff; only the filtered ~~JOYRAD-35~~ Ka Band data are included in the TRIPEx dataset. Note, that no such filtering is applied to the ~~KiXPol~~ X Band and ~~JOYRAD-94~~ W Band data.

~~One of the biggest challenges for multi-frequency observations is the match of radar volumes, which is negatively affected e.g. by horizontal instrument displacement, different radar beam widths and antenna pointing, and different range gates and temporal averaging. It is not trivial to accurately quantify these uncertainties, and their impact on multi-frequency studies also depends on the study target. For example, when analyzing cloud or precipitation structures with large vertical gradients (e.g., the melting layer) or high temporal variability, the volume mismatch effects will be larger than in studies of the usually more homogeneous ice clouds. In section 4.1 we provided some examples (Figure 5) on the application of error/quality flags and temporal averaging to mitigate these effects.~~

As described in Section 2.1, X Band was operated vertically pointing while rotating the antenna. Figure 7 illustrates effects related to imperfect vertical antenna pointing~~, which can be partly corrected for~~. When looking at differences ~~of~~ between vertical Doppler velocities ~~between observations~~ observed from low frequency and high frequency radars (Dual Doppler velocity, DDV), ~~we expect an increases of the difference due to non-Rayleigh scattering effects~~ increases are expected in presence of large scatterers (Matrosov, 2011; Kneifel et al., 2016). Large particles, which usually also have ~~larger~~ greater terminal ve-

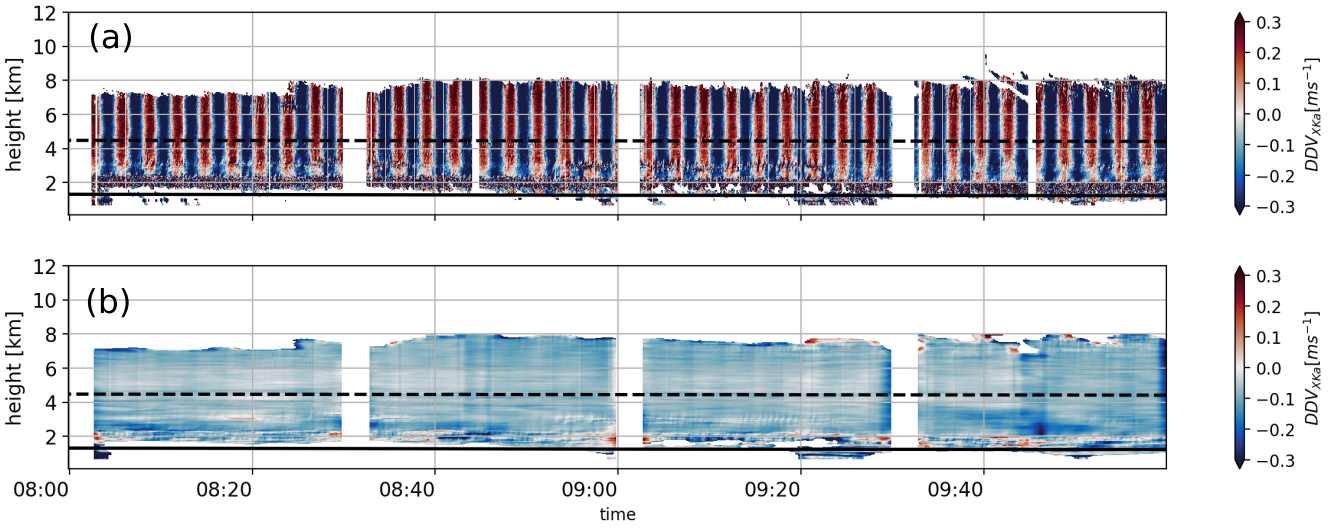

Figure 7. Time-height plots of the dual mean Doppler velocity using the Level 2 data of 20.11.2015. The dashed line and the continuous line are the ~~isotherm of~~ -15 and 0 °C isotherms, respectively. Panel ~~A~~ a shows the DDV_{XKa} using the original data from Level 2. Panel ~~B~~ b shows the DDV_{XKa} after applying ~~the~~ a 3 minutes moving average.

locities, ~~have~~ give a lower reflectivity signal at high frequencies due to non-Rayleigh scattering~~effects~~. This effect also leads to a ~~slightly~~ lower MDV (~~e.g~~ $MDV_X > MDV_{Ka} > MDV_W$). Since ~~we expect mostly Rayleigh scatterers~~ the ice particles in the uppermost ~~ice region of the cloud~~part of the clouds are expected to be Rayleigh scatterers, the DDV should ~~approach~~ be zero. However, ~~for~~ DDV_{XKa} (Panel ~~A~~ a of Figure 7) ~~we find~~ shows a periodic variation along the entire vertical range with the period matching the ~~KiXPol~~ X Band scan duration of 3 minutes. Obviously~~a non-prefect~~ , a non-perfect zenith pointing of the ~~KiXPol~~ X Band antenna introduces these periodic shifts in the mean Doppler velocity due to the contamination of the vertical Doppler signal by the horizontal wind component. ~~We estimated the optimal averaging time window to eliminate this effect to~~ A temporal average over 3 minutes ~~by minimizing~~ minimizes the standard deviation of DDV_{XKa} ~~using different~~ relative to other averaging window sizes (Panel ~~B~~ b of Figure 7). Note, that ~~we did not include~~ the averaged data is not included in the Level 2 data product, because the optimal averaging window ~~depends~~ might depend on the prevailing atmospheric, height-dependent wind conditions, and original data cannot be recovered after averaging. We can also not completely rule out a slight ~~mis-pointing~~ mispointing of the other two radars, because their DDVs sometimes show deviations especially in regions with strong horizontal winds with maximum DDVs~~, however,~~ . However, these DDVs are found to be below 0.4 ms^{-1}. An ad-hoc estimate of the related relative radar ~~mis-pointing~~ DIFdelend mispointing of the two radars using the horizontal wind information from radiosondes for a few extreme cases ~~suggest~~ suggests a potential mismatching of 0.5 °. A correction of the shift ~~should be possible when~~ requires reliable horizontal wind profiles~~are available, and it~~ , which will be investigated in more ~~details~~ detail in the future.

4.3 Radar sensitivity

Figure 8 shows the distribution of reflectivity values measured by the three radars during the entire campaign filtered with the error flags (bits 13, 14 and 15 in Table 4), and stratified by height above the site. As already mentioned, Ka Band and W Band show higher sensitivities compared to X Band up to high altitudes. Ka Band (Panel b in Figure 6) exhibits the largest dynamic range (Panels a and c in Figure 6). The step-like shape of the lowest altitude reflectivities from W Band is caused by different chirp settings (Table 2). A polynomial fit to the minimum retrieved linear reflectivities (Ze_{lin} in units of mm^6/m^3) as a function of altitude z (units of m),

$$Ze_{lin}(z) = a \cdot z^b \tag{2}$$

results for X and Ka Band in the expected nearly quadratic decrease with range (Table 6). The slower decrease (smaller exponent) for W Band results from the altitude-dependent sensitivity associated with the height-varying chirp settings.

The melting layer was mostly observed at altitudes between 1 and 2 km where it causes a sharper increase in the reflectivity distribution and the largest values measured for the X Band reflectivities. The X band Ze distribution shows an enhancement of the largest recorded values at 2 km from ≈30 dBZ to ≈40 dBZ. The X Band sensitivity limitations did not allow to observe signals above 7 km with reflectivities below -10 dBZ, however, dual-wavelength studies of clouds in this region are still possible with the W Band and Ka Band included in the Level 2 data. Nonetheless, ice aggregation and riming, which are most relevant for triple-frequency studies, usually occur at lower levels and larger reflectivities where all three radars provide sufficient sensitivity.

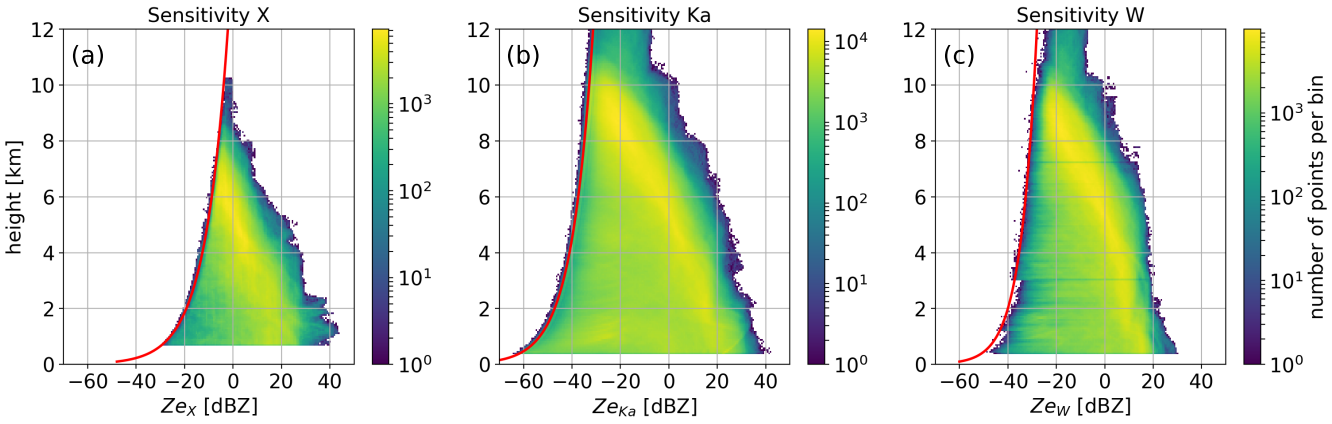

Figure 8. Histograms of reflectivities from the entire TRIPEx campaign Level 2 data for each radar. The red curve is the profile of the minimum retrieved reflectivity (Eq. 2). Panels a, b and c show the histograms for X, Ka and W Band, respectively; all error flags (see Tab. 4) were applied to filter the data. Note the log-scale on the colorbars.

Table 6. Coefficients a and b for the sensitivity fit (Eq. 2) obtained for X, Ka and W Band. The coefficients were calculated using the Level 2 dataset with a filtering according to the error flags applied (see Table 4).

Radar	a	b
X Band	$6.25 \cdot 10^{-10}$	2.19
Ka Band	$3.41 \cdot 10^{-12}$	2.04
W Band	$8.36 \cdot 10^{-10}$	1.53

5 Triple-frequency characteristics of ice and snow clouds

~~Long~~ Longer time series of observations are required in order to ~~corroborate the significance and~~ reliably estimate the occurrence ~~probability of certain~~ probabilities of process signatures in the triple-frequency space~~, which then can be used~~. Those statistics might be useful for the development of microphysical retrievals ~~. Profound statistics of typical triple-frequency signatures will also help to constrain the scattering models, which are required for such retrievals. The currently available experimental~~ and to constrain snow particle scattering models. Currently available datasets are restricted to short time periods or specific cases. Kulie et al. (2014) and Leinonen et al. (2012) used observations from airborne Ku, Ka and W Band radars data collected during the Wakasa Bay campaign (Lobl et al., 2007) ~~from Ku, Ka and W band airborne radars to evaluate the aggregate models~~ to evaluate aggregate and spheroidal snowflake models. Their ~~derived values for~~ $\mathrm{DWR_{KaW}}$ and $\mathrm{DWR_{KuKa}}$ values reach up to 10 dB and 8 dB, respectively. Although ~~the~~ their data are rather noisy due to volume mismatch and attenuation effects, ~~these were~~ they were the first observations which confirmed triple-frequency signatures ~~which were so far only~~ predicted by complex aggregate scattering models (Kneifel et al., 2011a). The first triple-frequency signatures from ground-based radars (~~C~~CS, Ka, W ~~band~~Band) were presented by ~~Stein et al. (2015)~~ Stein et al. (2015) for two case studies. Similar to the Wakasa Bay studies, they found deviation from predictions based on simpler spheroidal-based scattering models~~;~~, but their aggregates showed a $\mathrm{DWR_{KaW}}$ saturation around 8 dB and not ~~a~~ the 'hook' or 'bending back' feature ~~as~~ found in the previous studies. They ~~suggested~~ attributed this behaviour to ~~be closely connected to~~ a snow aggregate fractal dimension of two. ~~Kneifel et al. (2015)~~ Kneifel et al. (2015) combined triple-frequency ground-based radar (X, Ka and W ~~band~~Band) with in-situ observations, and analyzed three ~~case studies with~~ cases characterized by falling snow particles with different degrees of riming. For low density aggregates their $\mathrm{DWR_{KaW}}$ ~~is also not exceeding~~ did also not exceed the 8 dB limit reported by previous studies, but ~~in addition they found~~ exhibited a strong bending back feature (i.e., reduction of $\mathrm{DWR_{KaW}}$ for larger particles) with large $\mathrm{DWR_{XKa}}$ up to 15 dB. During riming periods, the triple-frequency signatures showed a distinctly different behavior~~.~~: $\mathrm{DWR_{KaW}}$ increases up to 10 dB, while $\mathrm{DWR_{XKa}}$ remains constant or slowly increases up to 3 dB, which appears in triple-frequency plots as an almost horizontal line.

The TRIPEx dataset is, to the best of our knowledge, one of the longest, quality-controlled triple-frequency ~~data collection~~ datasets currently available, which allows ~~to estimate the occurrence probability~~ for reliable estimations of the occurrence of several triple-frequency signatures in ~~mid-latitudes~~ mid-latitude winter clouds. In the following sections, we use the Level 2 data filtered only with the errors quality flag (see Table 4) to analyze the temperature dependence of the triple-frequency

signatures and signatures of riming and melting snow particles. The extension of the filtering to the warning flags would remove all melting layer cases and/or observations with larger amounts of super-cooled liquid water, which portray particularly interesting signatures of partially melted or rimed particles.

5.1 Temperature dependence of triple-frequency signatures

The large data set relatively large dataset allows us to stratify the occurrence probaility probability of DWR_{KaW} (Panel A a in Figure 9) and DWR_{XKa} (Panel B b in Figure 9) according to air temperature, which results in four main regimes. The regime between where the temperature is smaller than -20 and -15 °C exhibits constant DWRs small DWR values, mostly below 3 dB. In the regime between -15 and -7.5

Between -20 and -10 °C, we find a rapid widening of the distribution to higher values in both DWRs. This DWR increase becomes very rapid at temperatures warmer than -15 °C, which suggests an increasing number of larger aggregates caused by stronger aggregation due to preferential growth of dendritic particles around -15 in the -20 to -10 °C ; those particles temperature range (Kobayashi, 1957; Pruppacher and Klett, 1997). Dendrites are well known to favor snow aggregation due to their branched crystal structure. In accordance with previous studies, DWR_{KaW} saturates around 8 dB at -7.5 7 dB at -10 °C with only a small fraction reaching up to 10 dB. DWR_{XKa} approaches maximum values of 5 to 8 dB, however, the occurrence probability of enhanced DWR_{XKa} is smaller compared to those found for DWR_{KaW}. We expect this behavior as This is an expected behavior since early aggregation is expected likely to first enhance the DWR_{KaW} which is explained by the fact that growth of the particles first affect because particles growth early affects the high frequencies due to the transition from Rayleigh to non-Rayleigh regime. In our case, the W-Band which first transition out of the Rayleigh regime. Thus W Band radar is the first to be affect influenced by this transition producing an enhance of which enhances DWR_{KaW}.

At temperatures warmer than -7.5 and colder than between -10 and 0 °C, the distribution of DWR_{KaW} remains almost constant , except with the exception of a small peak with higher values around -5 °C and a widening of the distribution DWR distributions towards negative values. There are two main possible sources for this wideningThe latter effect might relate to two causes. The first is the inter radar calibration correction DWR calibration (Sec 3.5)where offset calculated to , derived for the upper part of the clouds , the ice part, was used to correct (ice part), which, when applied to the entire profilewhich may lead to overestimation of the , leads to the overestimation of Ze_W. The second possible source is the observation of different volumes by each radar due to a horizontal displacement and different range resolution; this effect is enhanced when the observed volumes are closer to the motivation is the radar . volume mismatch, which becomes worse for observations closer to the radars due to reduced overlap of the radar beams.

Interestingly, DWR_{XKa} grows continuously up to 12 dB from for temperatures warmer than -5 °C, which is in line with intensified aggregation of the snow particles towards lower heights. The very large DWR_{XKa} in this regime can be explained by the increase of increasing particle stickiness when approaching the 0 °C height. The fourth regime we define as regione level. In the fourth regime between 0 °C and the maximum in LDR . At this regime the DWR_{KaW} show a trend LDR maximum, DWR_{KaW} tends to further increase while the DWR_{XKa} remain constant or are about to decrease. The DWR_{KaW} assumes DWR_{XKa} remains

constant or even decreases. DWR_{KaW} reaches values up to 10 dB while ~~the DWR_{XKa} reaches~~ DWR_{XKa} attains values up to 15 dB which could be produced by ~~a persistent aggregationformation~~persistent aggregation.

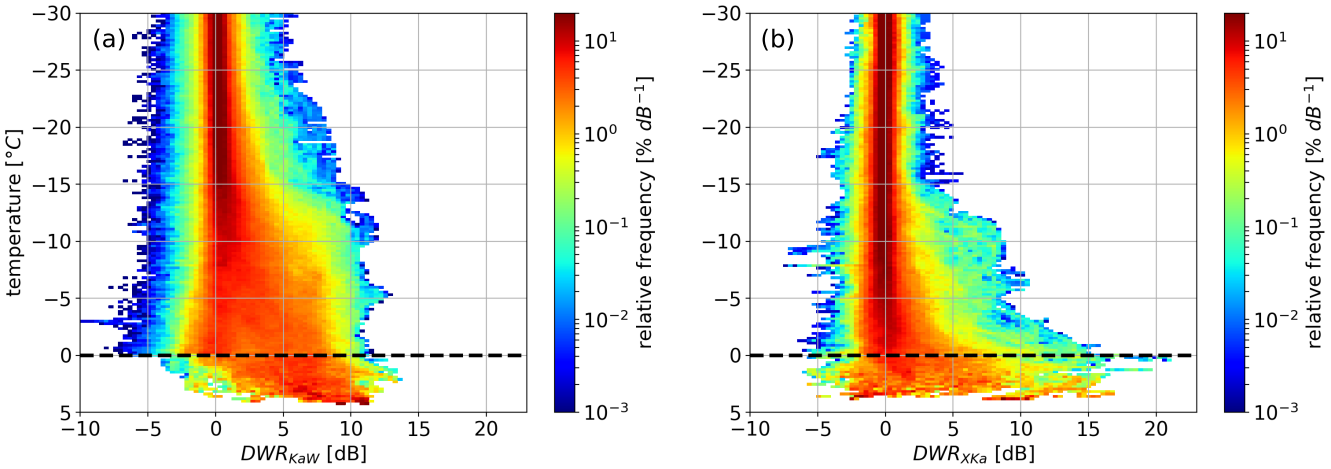

Figure 9. Two dimensional histograms (Contoured Frequency by Altitude Diagram ~~,~~(CFAD), see Yuter and Houze (1995) for more details) of DWR ~~as function of~~ against air temperature for the entire TRIPEx dataset. The dashed line indicates the ~~isotherm of~~ 0 °C isotherm. ~~Be aware that the~~ The data below the dashed line ~~is~~ are collected only ~~for~~ from the cases ~~when the~~ where a melting layer ~~was present~~is observed. The ~~DRWs~~ DWRs were filtered using the error flags and averaged in time using a 3 minutes moving ~~average~~window. Panels ~~A~~ a and ~~B~~ b show ~~the~~ DWR_{KaW} and DWR_{XKa}, respectively. Note the log-scale of the colorbars.

~~The~~ Figure 10 shows the triple-frequency ~~plots for the three temperature regimes unaffected by melting are shown in Figure 10 . Panel A shows the data from the first regime (~~plots for the temperature ranges -20 ~~to -15~~ < T < -10 °C ~~) where the majority of the points are distributed around 0 for both DWRs. At this region the growth of the particles is mostly by vapor deposition producing a slightly increase of DWR_{KaW} up to 7 . In Panel B, the data from the second regime (-15 to -7.5)are from the region where larger aggregates are likely generated in the dendritic growth layer. Similar to e. g. Stein et al. (2015), we find the typical bending or hook signature saturating at about a DWR~~ (panel a) and -10 < T < -1 °C (panel b). Between -20 and -10 °C (panel a), we find the typical bending signature in the triple-frequency space, saturating at about a DWR_{KaW} of 8 ~~.~~dB, similar to Stein et al. (2015). This temperature regime includes the Dendritic Growth Zone (DGZ), which is usually defined by cloud chamber experiments in the range of temperatures -17 to -12 °C (Kobayashi, 1957; Yamashtta et al., 1985; Takahashi, 2014). It is worth reminding that the temperature information, included in the TRIPEx dataset, has not been obtained from a direct measurement, but it has been taken from CloudNet. Consequently, it is not surprising that the growth regimes that we have identified using the signatures observed in the DWR profiles do not perfectly correspond in temperature to the ones determined in cloud chamber experiments.

Although we combine observations from different clouds, the variability of the triple-frequency signatures is relatively small. For warmer temperatures (~~-7.5~~ -10 to -1 °C~~(Panel C), where~~ , Panel b), needle aggregates are likely to be generated

and ice particles start to become more sticky ~~, the bending feature becomes more pronounced~~ leading to a more pronounced bending feature. For DWR_{XKa} reaching up to 12 dB~~also the bending back signature (reduction of DWR_{KaW} with increasing DWR_{XKa} as reported in Kneifel et al. (2015))~~ , also the hook (or bending back) signature (Kneifel et al., 2015) becomes visible for parts of the ~~data set~~dataset (DWR_{XKa} decreases while DWR_{KaW} is still increasing). This panel also reveals a secondary mode with DWR_{XKa} below 3 dB and DWR_{KaW} reaching up to 12 dB. Following ~~Kneifel et al. (2015)~~Kneifel et al. (2015), this mode could hint at rimed particles, which are still too small to enhance DWR_{XKa}, but due to their increased density and hence larger refractive index~~increase DWR_{KaW}~~ , the DWR_{KaW} increases. We will investigate this feature in more detail in the next subsection.

The dataset contains particularly large DWR signatures close to 0 °C and at higher temperatures, which ~~could be~~ are probably caused by melting snowflakes or simply by enhanced aggregation. To further investigate this signature we generated the triple-frequency plot for the data between the 0 °C and the height of the ~~maximum in the LDR~~ LDR maximum (Figure 11), which we consider as ~~a~~ proxy for the center of the melting layer (Le and Chandrasekar, 2013)~~(Figure 11)~~. In this region, DWR_{XKa} reaches maximum values up to 20 dB already at low DWR_{KaW}. Overall, the data points are much more scattered than those in the colder temperature regions~~, which also~~ . This larger variability might result from effects of the radar volume mismatch caused by ~~the stronger~~ strong vertical gradients near the melting layer~~; another possibility for this effect~~ . Another possible explanation is the much lower ~~number~~ amount of data. Latent heat release by melting increases turbulent ~~motions~~motion, which might further enhance the detrimental effects of volume mismatch. We need to be careful in interpreting these features as triple-frequency signatures of the melting layer, because the temperature information is based on CloudNet ~~product which obtains the temperature from ECMWF analysis~~ products taken from ECMWF analyses which cannot be expected to represent small scale variations of the 0 °C isotherm. Moreover, melting can be delayed depending on the ~~profile~~ profiles of temperature and humidity, and on the density and size of the particles themselves (Matsuo and Sasyo, 1981; Rasmussen and Pruppacher, 1982). A sagging of the melting layer has been repeatedly observed with the scanning polarimetric ~~X-band~~ X Band radar in Bonn (BoXPol, also part of JOYCE-CF) ~~in case of~~ for dominant riming processes (Xie et al., 2016; Trömel et al., 2018). Rimed particles fall with higher terminal velocities and ~~melt at lower heights~~consequently take more time to melt. In the following subsection, we will use LDR and the mean Doppler velocity to better separate non-melted from melted snow particles.

5.2 Signatures of riming and melting snow particles

During riming, super-cooled liquid water droplets freeze onto the ice particles~~, which~~ . This strongly increases the particle mass while its size grows ~~only~~ more slowly, especially during the onset of riming. Since the terminal velocity is mainly governed by the relation ~~of~~ between particle mass (gravitational force) and its cross section perpendicular to the air stream (drag force), its terminal ~~and~~ velocity observed by the mean Doppler velocity (MDV) ~~increase~~ increases due to riming ~~(Mosimann (1995))~~(Mosimann, 1995). MDVs above 1.5 ms^{-1} can be used as a simple indicator of rimed particles as long as vertical air ~~motions are small (e.g. Mosimann (1995)). The fraction~~ velocities are small (Mosimann, 1995). About 1% of triple-frequency data in the temperature range between -20 and -1 °C ~~with MDV larger than~~ have a MDV above 1.5 ms^{-1} ~~is about 1.3and displayed in Figure 12~~(Figure 12). Interestingly, we find one mode ~~which appears to be~~ very similar to a ~~line with~~

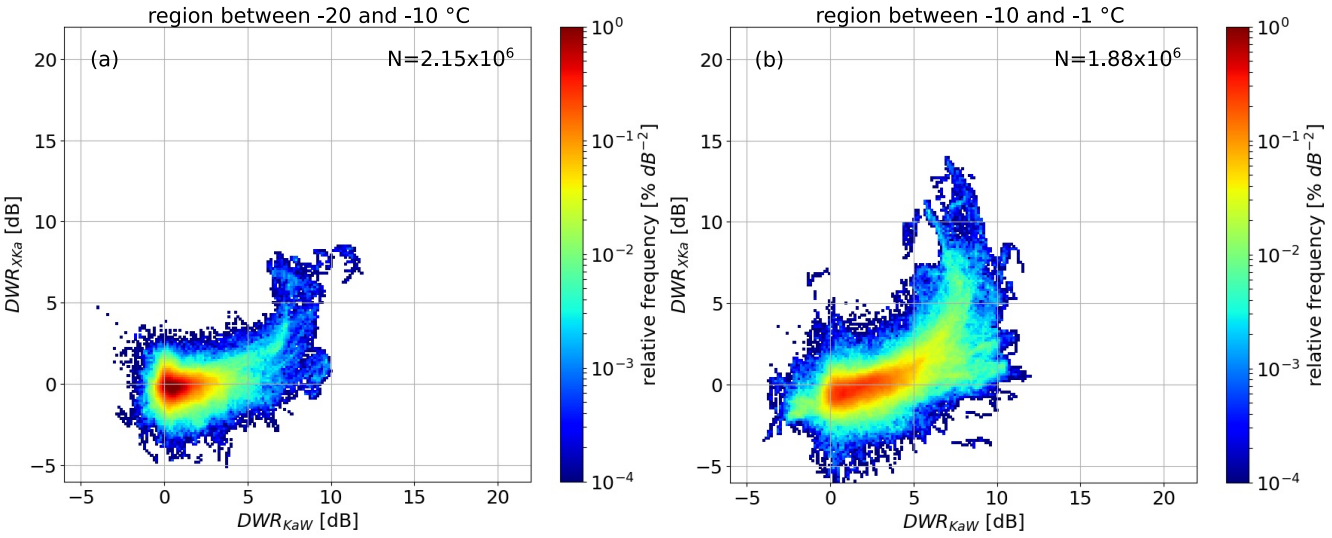

Figure 10. Two dimensional histogram of the triple frequency signatures for different temperature regions normalized by the total number of points N. The color shows the relative frequency. Panel ~~A~~ a is for ~~region between -20 and -15~~ temperatures lower than -17 °C; Panel ~~B~~ b shows the region between ~~-15~~ -17 °C and ~~-7.5~~ -7 °C; Panel ~~C~~ c illustrates data points lying between ~~-7.5~~ -7 °C and -1 °C. Note the log-scale on the colorbars.

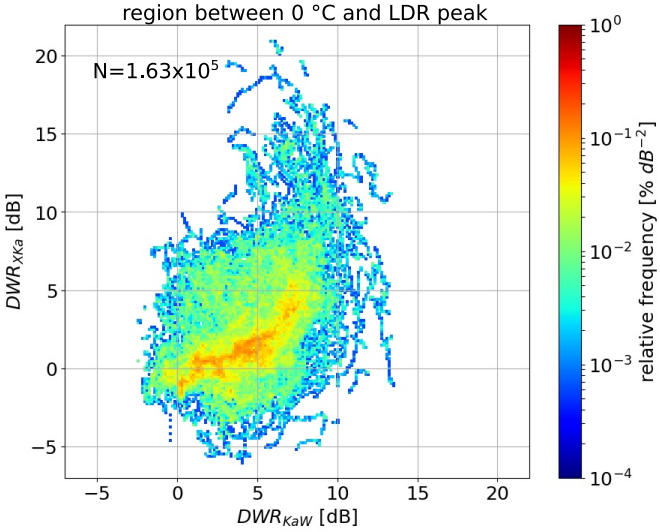

Figure 11. Two dimensional histogram of the triple frequency signatures for ~~a~~ the region between 0 °C and the ~~maximum of~~ LDR maximum in the melting layer normalized by the total number of points N. The color shows the relative frequency and the binning is matching what has been used for Figure 10. Note the log-scale on the colorbar.

~~low slope~~ sloped line found for rimed particles in ~~Kneifel et al. (2015)~~Kneifel et al. (2015), which coincides with large MDVs up to 2.4 ms^{-1} and $\mathrm{DWR}_{\mathrm{KaW}}$ up to 10 dB. However, the correlation between enhanced $\mathrm{DWR}_{\mathrm{KaW}}$ and MDV is less clear than in the case shown in ~~Kneifel et al. (2015)~~Kneifel et al. (2015). A more detailed investigation showed that TRIPEx contains only ~~two~~ short riming periods of a few minutes duration, while the period analyzed by ~~Kneifel et al. (2015) was considerable~~ Kneifel et al. (2015) was considerably longer (≈ 20 min). In general, $\mathrm{DWR}_{\mathrm{KaW}}$ is expected to increase for larger ~~particle sizes~~ particles and strong riming, but detailed sensitivity studies which clearly characterize these dependencies are still missing. Another mode in Figure 12 with larger $\mathrm{DWR}_{\mathrm{XKa}}$ of about 3 dB ~~suggest mean particles~~ suggests mean particle sizes exceeding 8 mm according to ~~Kneifel et al. (2015)~~Kneifel et al. (2015). We speculate ~~,~~ that this mode might be related to only slightly rimed aggregates. A larger number of riming events is required to better investigate the sensitivities of MDV and triple-frequency signatures to various degrees of riming, which also would be a very valuable basis to constrain theoretical particle models as ~~e.g. developed by Leinonen and Szyrmer (2015)~~developed for example by Leinonen and Szyrmer (2015).

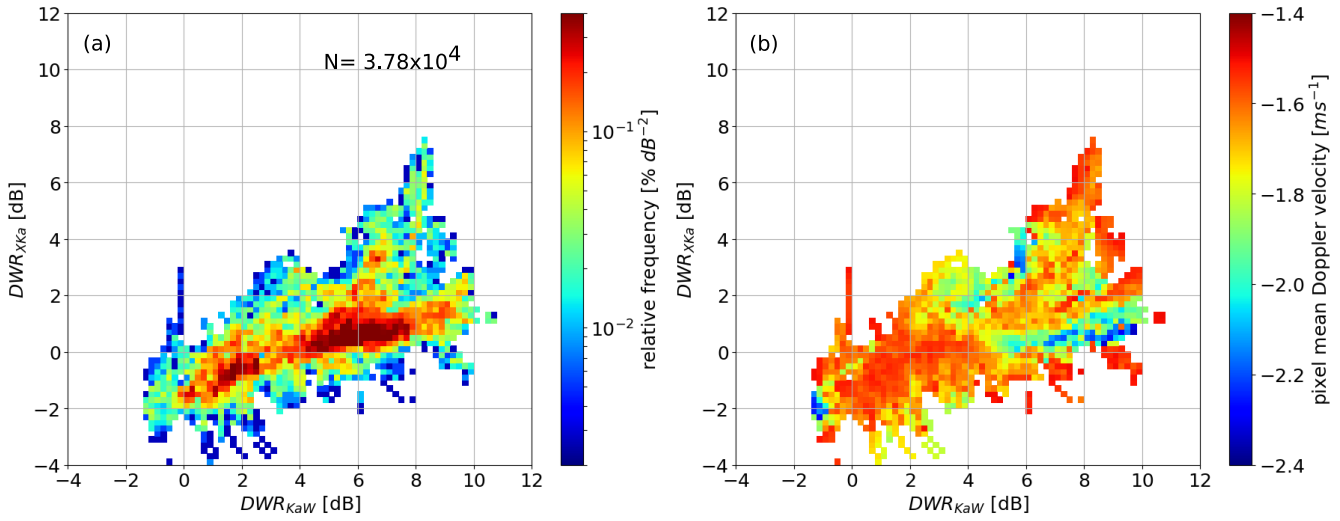

Figure 12. Triple frequency signatures for Level 2 data with temperatures between -20 and -1 °C and a mean Doppler velocity (MDV) above 1.5 ms^{-1} in order to select potentially ~~riming~~ rimed particles. Panel ~~A~~ a shows the relative frequency of the observations; Panel ~~B~~ b indicates the average MDV of each pixel in the histogram. Note the log-scale on the colorbar in A.

A particularly interesting signature shown in Figure 11 ~~are~~ is the very large $\mathrm{DWR}_{\mathrm{XKa}}$ close to the melting layer. To ~~the author's knowledge~~our knowledge, these features have not yet been described~~, nor is it clear~~. It is not clear to us whether these signatures are caused by very large aggregates or melting particles. A pure melting of snowflakes should enhance the MDV because of their decrease in size (and thus cross sectional area) ~~and~~ as well as drag in the airflow. Early melting can, however, be better detected by LDR: the much larger refractive index of liquid water compared to ice and the initially still asymmetric melting ~~snowflake~~ snowflakes result in a much larger depolarization signal as ~~for the dry snowflake~~compared to dry snowflakes. Hence, we re-plot Figure 11 ~~. One can clearly~~ to better see the transition from dry snowflakes with a typical MDV of 1 ms^{-1}

and LDR ~~values~~ around -15 dB to larger MDV ~~and coinciding~~ coinciding with rising LDR as expected for melted snow. Interestingly, the very large DWR_{XKa} show mostly MDV and LDR values associated ~~to~~ with unmelted snowflakes. Once the MDV and LDR indicate the onset of melting, the ~~DWR, especially the~~ DWRs, especially DWR_{XKa}, rapidly decrease. As ~~the~~ DWR_{XKa} is strongly related to the mean particle size, the results indicate that the largest snowflake sizes occur before the melting starts. Once ~~the~~ snowflakes are completely melted, ~~the~~ DWR_{KaW} will be still enhanced due to ~~non-Rayleigh scattering of the raindrops but the~~ Mie scattering by the raindrops while DWR_{XKa} will ~~be~~ remain close to 0 dB (Tridon et al., 2017). However, our corrections for attenuation within the melting layer are certainly incomplete, thus we leave a deeper analysis of that feature to future studies.

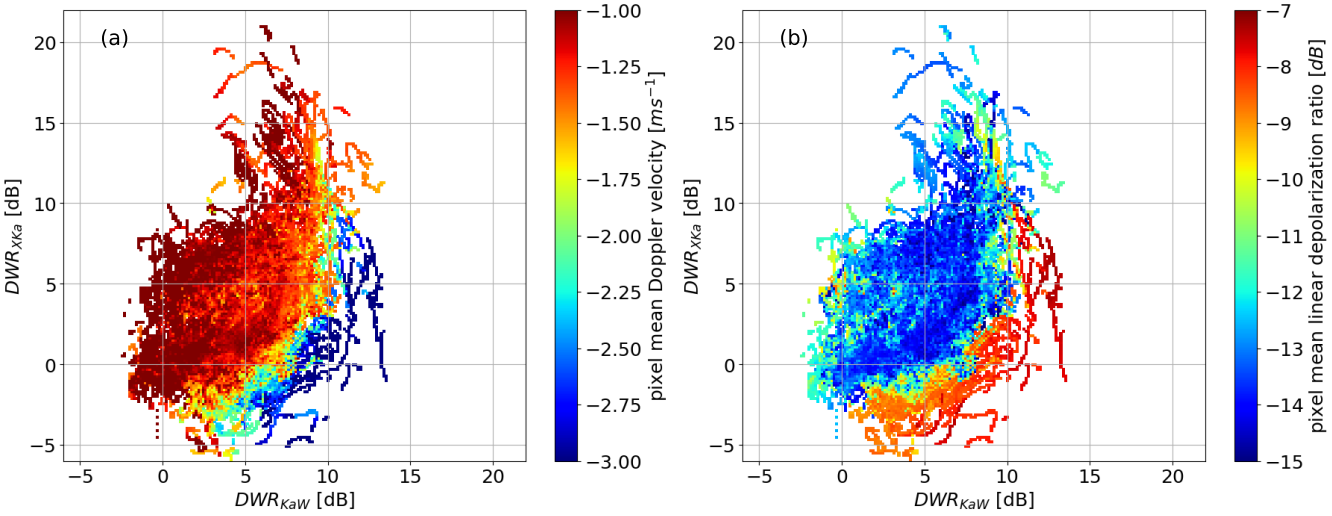

Figure 13. Triple-frequency diagrams of observations between 0 °C and the ~~maximum of~~ LDR maximum in the melting layer (same as Panel ~~C~~ c of Figure 10), but the color in Panel ~~A~~ a indicates the average MDV while in Panel ~~B~~ b the color shows the average LDR.

6 Conclusions

~~This paper presents the first long-term dataset (two months)~~ We present the first two-month long dataset of vertically pointing triple-frequency Doppler radar (X, Ka, and ~~W-Band~~W Band) observations of winter clouds at a mid-latitude site (JOYCE-CF, Jülich, Germany)~~, and it describes the~~ . The dataset includes spatio-temporal ~~re-gridding of the data as well as the~~ re-gridded data including offset and attenuation corrections~~applied~~. Several quality flags ~~are developed which enables~~ allow to filter the dataset according to the needs of the specific application. The quality flags have been separated into error and warning flags; we recommend to always apply the error flags, while the warning flags might not be necessary depending on the ~~case or the focus of the analysis~~application. All corrections applied are ~~separately stored~~ stored separately in the data files in order to allow the user to recover and work also with data at intermediate processing steps and to potentially apply individual ~~and other~~

corrections. This might be necessary ~~as our~~ because the campaign focus was on the ice and snow part of the cloud~~and hence, for example~~. Consequently, the correction for path integrated attenuation, might be inappropriate for example for studies investigating the melting layer or rainfall.

The statistical analysis of the ice part of the clouds revealed dominant triple-frequency signatures related to aggregation (hook or bending up feature). In agreement with previous studies, DWR_{KaW} mostly saturates around ~~8~~ 7 dB while DWR_{XKa} reaches values of up to 20 dB in regions of presumably intense aggregation close to the melting layer. Due to the large dataset, we were able to investigate the relation between the DWRs and temperature. The first significant increase of aggregation starts ~~at~~ around -15 °C where ~~plate-like and~~ dendritic crystals are known to grow efficiently and favour aggregation. In this zone, DWR_{KaW} mostly increases up to its saturation value of ~~8~~ 7 dB~~while~~. DWR_{XKa} increases mainly below ~~-7.5~~ -10 °C. Close to the melting layer, DWR_{XKa} massively increases up to ~~extreme values of~~ 20 dB, which has not been reported so far. A ~~further~~ deeper investigation using LDR and MDV revealed that these extreme DWR_{XKa} are indeed due to large dry aggregates rather than melting particles~~, which cause the DWR_{XKa} to decrease. This finding suggests future studies of the aggregation processes within or close to the melting layer, but also scattering computations of melting particles~~. Once melting is indicated by larger MDV and LDR, DWR_{XKa} appears to rapidly decrease. Clearly, combined observational and scattering modeling studies are needed to further investigate this transition. Although the dataset contains only a few short riming periods (approximately ~~1.3~~1% of the data between -20 and -1 °C), a simple MDV threshold reveals the typical riming signature (flat horizontal line in the triple-frequency space) reported for riming case studies in Kneifel et al. (2015). The statistical analysis of riming is more challenging ~~as~~ compared to aggregation. Riming is often connected to larger amounts of super-cooled liquid water, larger vertical air motions, and turbulence, which deteriorate the signal due to liquid water attenuation and enhance effects of imperfect radar volume matching. Riming could be further investigated with this dataset ~~when concentrating on specific caseswhere~~ by focusing on single cases, for which it is possible to apply specific corrections and filtering~~can be applied~~.

The synergy with nearby polarimetric weather radar observations will be investigated in future studies by including the vertical polarimetric profiles matching the JOYCE-CF site based on Quasi-Vertical Profiles (QVPs) ~~(e.g. Trömel et al. (2014); Ryzhkov et al. (20~~ (Trömel et al., 2014; Ryzhkov et al., 2016) or Columnar Vertical Profiles (CVPs) (Murphy et al., 2017; Trömel et al., 2018). Also a data release including the W and Ka Band Radar Doppler spectra is planned.

7 Data availability

The TRIPEx Level 2 data are available for download at the ZENODO platform (https://doi.org/10.5281/zenodo.1341389). Quicklooks of the TRIPEx dataset are freely accessible via a data quicklook browser (http://gop.meteo.uni-koeln.de/~Hatpro/dataBrowser/dataBrowser1.html?site=TRIPEX&date=2015-11-20&UpperLeft=3radar_Ze). The raw and Level 1 data and K_{dp} can be requested from the corresponding author.

Competing interests. The authors declare that they have no conflict of interest.

Acknowledgements. The authors acknowledge the funding provided by the German Research Foundation (DFG) under grant KN 1112/2-1 as part of the Emmy-Noether Group OPTIMIce. JD also acknowledges support by the Graduate School of Geosciences of the University of Cologne. We thank the departments S, G and IEK-7 for the technical and administrative support during the field experiment. The majority of data for this dataset were obtained at the JOYCE Core Facility (JOYCE-CF) co-funded by DFG under DFG reserach grant LO 901/7-1. Major instrumentation at the JOYCE site was funded by the Transregional Collaborative Research Center TR32 (Simmer et al., 2015) funded by DFG, and JuXPol by the TERENO (Terrestrial Environmental Observatories) program of the Helmholtz Association (Zacharias et al., 2011). For this work, we used products obtained within the Cloudnet project (part of the EU H2020 project ACTRIS (European Research Infrastructure for the observation of Aerosol, Clouds, and Trace gases)) and developed during the High Definition Clouds and Precipitation for advancing Climate Prediction $\mathrm{HD(CP)}^2$ project funded by the German Ministry for Education and Research under grants 01LK1209B and 01LK1502E.

References

Baldini, L. and Gorgucci, E.: Identification of the Melting Layer through Dual-Polarization Radar Measurements at Vertical Incidence, Journal of Atmospheric and Oceanic Technology, 23, 829–839, https://doi.org/10.1175/JTECH1884.1, 2006.

Chase, R. J., Finlon, J. A., Borque, P., McFarquhar, G. M., Nesbitt, S. W., Tanelli, S., Sy, O. O., Durden, S. L., and Poellot, M. R.: Evaluation of Triple-Frequency Radar Retrieval of Snowfall Properties Using Coincident Airborne In Situ Observations During OLYMPEX, Geophysical Research Letters, 45, 5752–5760, https://doi.org/10.1029/2018GL077997, 2018.

Diederich, M., Ryzhkov, A., Simmer, C., Zhang, P., and Trömel, S.: Use of Specific Attenuation for Rainfall Measurement at X-Band Radar Wavelengths. Part I: Radar Calibration and Partial Beam Blockage Estimation, Journal of Hydrometeorology, 16, 487–502, https://doi.org/10.1175/JHM-D-14-0066.1, 2015.

Gergely, M., Cooper, S. J., and Garrett, T. J.: Using snowflake surface-area-to-volume ratio to model and interpret snowfall triple-frequency radar signatures, Atmospheric Chemistry and Physics, 17, 12 011–12 030, https://doi.org/10.5194/acp-17-12011-2017, 2017.

Görsdorf, U., Lehmann, V., Bauer-Pfundstein, M., Peters, G., Vavriv, D., Vinogradov, V., and Volkov, V.: A 35-GHz polarimetric doppler radar for long-term observations of cloud parameters-description of system and data processing, Journal of Atmospheric and Oceanic Technology, 32, 675–690, https://doi.org/10.1175/JTECH-D-14-00066.1, 2015.

Grecu, M., Tian, L., Heymsfield, G. M., Tokay, A., Olson, W. S., Heymsfield, A. J., Bansemer, A., Grecu, M., Tian, L., Heymsfield, G. M., Tokay, A., Olson, W. S., Heymsfield, A. J., and Bansemer, A.: Nonparametric Methodology to Estimate Precipitating Ice from Multiple-Frequency Radar Reflectivity Observations, Journal of Applied Meteorology and Climatology, 57, 2605–2622, https://doi.org/10.1175/JAMC-D-18-0036.1, 2018.

Hogan, R. J., Illingworth, A. J., and Sauvageot, H.: Measuring crystal size in cirrus using 35- and 94-GHz radars, Journal of Atmospheric and Oceanic Technology, 17, 27–37, https://doi.org/10.1175/1520-0426(2000)017<0027:MCSICU>2.0.CO;2, 2000.

Hogan, R. J., Gaussiat, N., and Illingworth, A. J.: Stratocumulus Liquid Water Content from Dual-Wavelength Radar, Journal of Atmospheric and Oceanic Technology, 22, 1207–1218, https://doi.org/10.1175/JTECH1768.1, 2005.

Hou, A., Kakar, R., Neeck, S., Azarbarzin, A., Kummerow, C., Kojima, M., Oki, R., Nakamura, K., and Iguchi, T.: The Global Precipitation Measurement Mission, Bulletin of the American Meteorological Society, 95, 701–722, https://doi.org/10.1175/BAMS-D-13-00164.1, 2014.

Huang, G.-J., Bringi, V. N., and Thurai, M.: Orientation Angle Distributions of Drops after an 80-m Fall Using a 2D Video Disdrometer, Journal of Atmospheric and Oceanic Technology, 25, 1717–1723, https://doi.org/10.1175/2008JTECHA1075.1, 2008.

Illingworth, A. J., Hogan, R. J., O'Connor, E. J., Bouniol, D., Brooks, M. E., Delanoë, J., Donovan, D. P., Eastment, J. D., Gaussiat, N., Goddard, J. W. F., Haeffelin, M., Klein Baltinik, H., Krasnov, O. A., Pelon, J., Piriou, J. M., Protat, A., Russchenberg, H. W. J., Seifert, A., Tompkins, A. M., van Zadelhoff, G. J., Vinit, F., Willen, U., Wilson, D. R., and Wrench, C. L.: Cloudnet: Continuous evaluation of cloud profiles in seven operational models using ground-based observations, Bulletin of the American Meteorological Society, 88, 883–898, https://doi.org/10.1175/BAMS-88-6-883, 2007.

Kalthoff, N., Adler, B., Wieser, A., Kohler, M., Träumner, K., Handwerker, J., Corsmeier, U., Khodayar, S., Lambert, D., Kopmann, A., Kunka, N., Dick, G., Ramatschi, M., Wickert, J., and Kottmeier, C.: KITcube - a mobile observation platform for convection studies deployed during HyMeX, Meteorologische Zeitschrift, 22, 633–647, http://dx.doi.org/10.1127/0941-2948/2013/0542, 2013.

Kneifel, S., Kulie, M. S., and Bennartz, R.: A triple-frequency approach to retrieve microphysical snowfall parameters, Journal of Geophysical Research Atmospheres, 116, 1–15, https://doi.org/10.1029/2010JD015430, 2011a.

Kneifel, S., Maahn, M., Peters, G., and Simmer, C.: Observation of snowfall with a low-power FM-CW K-band radar (Micro Rain Radar), Meteorology and Atmospheric Physics, 113, 75–87, https://doi.org/10.1007/s00703-011-0142-z, 2011b.

Kneifel, S., von Lerber, A., Tiira, J., Moisseev, D., Kollias, P., and Leinonen, J.: Observed relations between snowfall microphysics and triple-frequency radar measurements, Journal of Geophysical Research: Atmospheres, 120, 6034–6055, https://doi.org/10.1002/2015JD023156, 2015.

Kneifel, S., Kollias, P., Battaglia, A., Leinonen, J., Maahn, M., Kalesse, H., and Tridon, F.: First observations of triple-frequency radar Doppler spectra in snowfall: Interpretation and applications, Geophysical Research Letters, 43, 2225–2233, https://doi.org/10.1002/2015GL067618, 2016.

Kobayashi, T.: Experimental Researches en the Snow Crystal Habit and Growth by Means of a Diffusion Cloud Chamber, Journal of the Meteorological Society of Japan. Ser. II, 35A, 38–47, https://doi.org/10.2151/jmsj1923.35A.0_38, 1957.

Küchler, N., Kneifel, S., Löhnert, U., Kollias, P., Czekala, H., and Rose, T.: A W-band radar-radiometer system for accurate and continuous monitoring of clouds and precipitation, Journal of Atmospheric and Oceanic Technology, 34, 2375–2392, https://doi.org/10.1175/JTECH-D-17-0019.1, 2017.

Kulie, M. S., Hiley, M. J., Bennartz, R., Kneifel, S., and Tanelli, S.: Triple-Frequency Radar Reflectivity Signatures of Snow: Observations and Comparisons with Theoretical Ice Particle Scattering Models, J. Appl. Meteorol. Climatol., 53, 1080–1098, 2014.

Le, M. and Chandrasekar, V.: Hydrometeor profile characterization method for dual-frequency precipitation radar onboard the GPM, IEEE Transactions on Geoscience and Remote Sensing, 51, 3648–3658, https://doi.org/10.1109/TGRS.2012.2224352, 2013.

Leinonen, J.: High-level interface to T-matrix scattering calculations: architecture, capabilities and limitations, Opt. Express, 22, 1655–1660, https://doi.org/10.1364/OE.22.001655, 2014.

Leinonen, J. and Moisseev, D.: What do triple-frequency radar signatures reveal about aggregate snowflakes?, J. Geophys. Res., 120, 229–239, http://dx.doi.org/10.1002/2014JD022072, 2015.

Leinonen, J. and Szyrmer, W.: Radar signatures of snowflake riming: a modeling study, Earth and Space Science, pp. 2333–5084, https://doi.org/10.1002/2015EA000102, 2015.

Leinonen, J., Kneifel, S., Moisseev, D., Tyynelä, J., Tanelli, S., and Nousiainen, T.: Evidence of nonspheroidal behavior in millimeter-wavelength radar observations of snowfall, Journal of Geophysical Research Atmospheres, 117, 1–10, https://doi.org/10.1029/2012JD017680, 2012.

Leinonen, J., Lebsock, M. D., Tanelli, S., Sy, O. O., Dolan, B., Chase, R. J., Finlon, J. A., von Lerber, A., and Moisseev, D.: Retrieval of snowflake microphysical properties from multifrequency radar observations, Atmospheric Measurement Techniques, 11, 5471–5488, https://doi.org/10.5194/amt-11-5471-2018, 2018.

Lobl, E. S., Aonashi, K., Murakami, M., Griffith, B., Kummerow, C., Liu, G., and Wilheit, T.: Wakasa bay, Organization, pp. 551–558, https://doi.org/10.1175/BAMS-88-4-551, 2007.

Löffler-Mang, M. and Joss, J.: An optical disdrometer for measuring size and velocity of hydrometeors, Journal of Atmospheric and Oceanic Technology, 17, 130–139, https://doi.org/10.1175/1520-0426(2000)017<0130:AODFMS>2.0.CO;2, 2000.

Löhnert, U., Schween, J. H., Acquistapace, C., Ebell, K., Maahn, M., Barrera-Verdejo, M., Hirsikko, A., Bohn, B., Knaps, A., O'Connor, E., Simmer, C., Wahner, A., and Crewell, S.: JOYCE: Jülich Observatory for Cloud Evolution, Bulletin of the American Meteorological Society, 96, 1157–1174, https://doi.org/10.1175/BAMS-D-14-00105.1, 2015.

Maahn, M., Löhnert, U., Kollias, P., Jackson, R. C., and McFarquhar, G. M.: Developing and evaluating ice cloud parameterizations for forward modeling of radar moments using in situ aircraft observations, Journal of Atmospheric and Oceanic Technology, 32, 880–903, https://doi.org/10.1175/JTECH-D-14-00112.1, 2015.

Macke, A., Seifert, P., Baars, H., Barthlott, C., Beekmans, C., Behrendt, A., Bohn, B., Brueck, M., Bühl, J., Crewell, S., Damian, T., Deneke, H., Düsing, S., Foth, A., Di Girolamo, P., Hammann, E., Heinze, R., Hirsikko, A., Kalisch, J., Kalthoff, N., Kinne, S., Kohler, M., Löhnert, U., Madhavan, B. L., Maurer, V., Muppa, S. K., Schween, J., Serikov, I., Siebert, H., Simmer, C., Späth, F., Steinke, S., Träumner, K., Trömel, S., Wehner, B., Wieser, A., Wulfmeyer, V., and Xie, X.: The HD(CP)^2 Observational Prototype Experiment (HOPE) – an overview, Atmospheric Chemistry and Physics, 17, 4887–4914, https://doi.org/10.5194/acp-17-4887-2017, 2017.

Matrosov, S. Y.: Possibilities of cirrus particle sizing from dual-frequency radar measurements, Journal of Geophysical Research, 98, 20 675, https://doi.org/10.1029/93JD02335, 1993.

Matrosov, S. Y.: A dual-wavelength radar method to measure snowfall rate, J. Appl. Meteorol., 37, 1510–1521, https://doi.org/10.1175/1520-0450(1998)037<1510:ADWRMT>2.0.CO;2, 1998.

Matrosov, S. Y.: Feasibility of using radar differential Doppler velocity and dual-frequency ratio for sizing particles in thick ice clouds, Journal of Geophysical Research, 116, D17 202, https://doi.org/10.1029/2011JD015857, 2011.

Matsuo, T. and Sasyo, Y.: Melting of Snowflakes below Freezing Level in the Atmosphere, Journal of the Meteorological Society of Japan. Ser. II, 59, 10–25, https://doi.org/10.2151/jmsj1965.59.1_10, 1981.

Mosimann, L.: An improved method for determining the degree of snow crystal riming by vertical Doppler radar, Atmospheric Research, 37, 305–323, https://doi.org/10.1016/0169-8095(94)00050-N, 1995.

Murphy, A., Ryzhkov, A., Zhang, P., McFarquhar, G., Wu, W., and Stechman, D.: A Polarimetric and Microphysical Analysis of the Stratiform Rain Region of MCSs, in: 38th Conference on Radar Meteorology, Chicago, Illinois, USA, 2017.

Pruppacher, H. R. and Klett, J. D.: Microphysics of Clouds and Precipitation, p. 954, Springer, Dordrecht, https://doi.org/https://doi.org/10.1007/978-0-306-48100-0, 1997.

Rasmussen, R. and Pruppacher, H. R.: A wind tunnel and theoretical study of the melting behavior of atmospheric ice particles I: A wind tunnel study of frozen drops of radius < 500 μm, https://doi.org/10.1175/1520-0469(1982)039<0152:AWTATS>2.0.CO;2, 1982.

Rosenkranz, P. W.: Atmospheric Remote Sensing by Microwave Radiometry, chap. 2, Wiley, New York, 1993.

Rosenkranz, P. W.: Water vapor microwave continuum absorption: A comparison of measurements and models, Radio Science, 33, 919–928, http://doi.wiley.com/10.1029/98RS01182, 1998.

Rosenkranz, P. W.: Correction [to "Water vapor microwave continuum absorption: A comparison of measurements and models" by Philip W. Rosenkranz], Radio Science, 34, 1025–1025, https://doi.org/10.1029/1999RS900020, 1999.

Ryzhkov, A., Zhang, P., Reeves, H., Kumjian, M., Tschallener, T., Trömel, S., and Simmer, C.: Quasi-vertical profiles-A new way to look at polarimetric radar data, Journal of Atmospheric and Oceanic Technology, 33, 551–562, https://doi.org/10.1175/JTECH-D-15-0020.1, 2016.

Simmer, C., Thiele-Eich, I., Masbou, M., Amelung, W., Bogena, H., Crewell, S., Diekkrüger, B., Ewert, F., Hendricks Franssen, H.-J., Huisman, J. A., Kemna, A., Klitzsch, N., Kollet, S., Langensiepen, M., Löhnert, U., Rahman, A. S. M. M., Rascher, U., Schneider, K., Schween, J., Shao, Y., Shrestha, P., Stiebler, M., Sulis, M., Vanderborght, J., Vereecken, H., van der Kruk, J., Waldhoff, G., and Zerenner, T.: Monitoring and Modeling the Terrestrial System from Pores to Catchments: The Transregional Collaborative Research Center on Patterns in the Soil–Vegetation–Atmosphere System, Bulletin of the American Meteorological Society, 96, 1765–1787, https://doi.org/10.1175/BAMS-D-13-00134.1, 2015.

Stein, T. H., Westbrook, C. D., and Nicol, J. C.: Fractal geometry of aggregate snowflakes revealed by triple-wavelength radar measurements, Geophysical Research Letters, 42, 176–183, https://doi.org/10.1002/2014GL062170, 2015.

Takahashi, T.: Influence of Liquid Water Content and Temperature on the Form and Growth of Branched Planar Snow Crystals in a Cloud, Journal of the Atmospheric Sciences, 71, 4127–4142, https://doi.org/10.1175/JAS-D-14-0043.1, 2014.

Thurai, M., Huang, G. J., Bringi, V. N., Randeu, W. L., and Schönhuber, M.: Drop Shapes, Model Comparisons, and Calculations of Polarimetric Radar Parameters in Rain, Journal of Atmospheric and Oceanic Technology, 24, 1019–1032, https://doi.org/10.1175/JTECH2051.1, 2007.

Tridon, F., Battaglia, A., Luke, E., and Kollias, P.: Rain retrieval from dual-frequency radar Doppler spectra: validation and potential for a mid-latitude precipitating case-study, Quarterly Journal of the Royal Meteorological Society, 143, 1364–1380, https://doi.org/10.1002/qj.3010, 2017.

Trömel, S., Ryzhkov, A. V., Zhang, P., and Simmer, C.: Investigations of backscatter differential phase in the melting layer, Journal of Applied Meteorology and Climatology, 53, 2344–2359, https://doi.org/10.1175/JAMC-D-14-0050.1, 2014.

Trömel, S., Ryzhkov, A., Hickman, B., Mühlbauer, K., and Simmer, C.: Climatology of the vertical profiles of polarimetric radar variables at X band in stratiform clouds, Submitted to Journal of Applied Meteorology and Climatology, 2018.

Tyynelä, J. and Chandrasekar, V.: Characterizing falling snow using multifrequency dual-polarization measurements, J. Geophys. Res., 119, https://doi.org/10.1002/2013JD021369, 2014.

Xie, X., Evaristo, R., Simmer, C., Handwerker, J., and Trömel, S.: Precipitation and microphysical processes observed by three polarimetric X-band radars and ground-based instrumentation during HOPE, Atmospheric Chemistry and Physics, 16, 7105–7116, https://doi.org/10.5194/acp-16-7105-2016, 2016.

Yamashtta, T., Asano, A., and Ohno, T.: Comparison of Ice Crystals Grown from Vapour in Varying Conditions, Annals of Glaciology, 6, 242–245, https://doi.org/10.3189/1985AoG6-1-242-245, 1985.

Yin, M., Liu, G., Honeyager, R., and Joseph Turk, F.: Observed differences of triple-frequency radar signatures between snowflakes in stratiform and convective clouds, Journal of Quantitative Spectroscopy and Radiative Transfer, 193, 13–20, https://doi.org/10.1016/J.JQSRT.2017.02.017, 2017.

Yuter, S. E. and Houze, R. A.: Three-Dimensional Kinematic and Microphysical Evolution of Florida Cumulonimbus. Part II: Frequency Distributions of Vertical Velocity, Reflectivity, and Differential Reflectivity, Monthly Weather Review, 123, 1941–1963, https://doi.org/10.1175/1520-0493(1995)123<1941:TDKAME>2.0.CO;2, 1995.

Zacharias, S., Bogena, H., Samaniego, L., Mauder, M., Fuß, R., Pütz, T., Frenzel, M., Schwank, M., Baessler, C., Butterbach-Bahl, K., Bens, O., Borg, E., Brauer, A., Dietrich, P., Hajnsek, I., Helle, G., Kiese, R., Kunstmann, H., Klotz, S., Munch, J. C., Papen, H., Priesack, E., Schmid, H. P., Steinbrecher, R., Rosenbaum, U., Teutsch, G., and Vereecken, H.: A Network of Terrestrial Environmental Observatories in Germany, Vadose Zone Journal, 10, 955, https://doi.org/10.2136/vzj2010.0139, 2011.

Zrnić, D. S., Raghavan, R., and Chandrasekar, V.: Observations of Copolar Correlation Coefficient through a Bright Band at Vertical Incidence, Journal of Applied Meteorology, 33, 45–52, https://doi.org/10.1175/1520-0450(1994)033<0045:OOCCCT>2.0.CO;2, 1994.